Supporting Information for

Interfacial Water Regulation Enables Stable Ampere-Level Nitrate to Ammonia Conversion

Xinyue Shi[1†], Wei-Hsiang Huang[2,3†], Xingkao Zhang[4†], Minghui Xie[1†], Toshinari Koketsu[5,6], Ping Zhang[1], Yiming Zhu[7], Xuepeng Zhong[5], Xiaoyan Zhou[1], Jun Chen[8], Min-Hsin Yeh[2,9], Xiaohua Yu[4*], Peter Strasser[5*], Jiwei Ma[1*], Hongfei Cheng[1*]

Methods

Chemical reagents

Nickel sulfate heptahydrate ($NiSO_4 \cdot 7H_2O$, ≥ 98%), sodium citrate ($C_6H_5O_7Na_3$, ≥ 98%), salicylic acid ($C_7H_6O_3$, ≥ 99.5%), sodium nitroferricyanide dihydrate ($Na_2[Fe(CN)_5NO] \cdot 2H_2O$, ≥ 99%), and sodium hypochlorite aqueous solution (NaClO, 6-14%) were supplied by Aladdin. Ferric sulfate ($Fe_2(SO_4)_3$, > 99%), sodium nitrite ($NaNO_2$, ≥ 99.99%), N-(1-naphthyl) ethylenediamine dihydrochloride ($C_{12}H_{16}C_{l2}N_2$, 99%), p-dimethylaminobenzaldehyde ($C_9H_{11}NO$, 99%), and maleic acid ($C_4H_4O_4$, 99%) were obtained from Adamas-beta. Aqueous silver nitrate solution ($AgNO_3$, 1 mol L^{-1}) and ammonium chloride aqueous solution (NH_4Cl, 0.1 g L^{-1}) were purchased from North Weiye Measurement Group Co., Ltd. Potassium nitrate (KNO_3, ≥ 99%), phosphoric acid (H_3PO_4, 85%), nitric acid (HNO_3, 65-68%), sulfuric acid (H_2SO_4, 95-98%), and hydrogen peroxide (H_2O_2, ≥ 30%) were procured from Sinopharm Chemical Reagent Co. Ltd (Shanghai, China). Potassium hydroxide (KOH, 85%) and potassium nitrate-^{15}N ($K^{15}NO_3$, ≥99 at.% 15N, ≥ 99%) were obtained from Innochem. Toray Carbon Paper (CP, TGP-H-60) and Nafion 211 membrane were sourced from the Sci materials hub. Platinum electrode clamp, platinum sheet electrode, graphite rod electrode, Ag/AgCl (saturated KCl) reference electrode, and Hg/HgO (1 M KOH) reference electrode were supplied from Tianjin Aida Hengsheng Technology Development Co., Ltd. Membrane electrode assembly device (MEA) was purchased from Gaossunion Technology Co., Ltd. All reagents were employed as received, with no additional purification.

Catalyst preparation

Carbon paper (CP) was employed as the substrate for catalyst fabrication via electrodeposition in a three-electrode system. The CP was sequentially cleaned by ultrasonication in anhydrous ethanol (30 min), 5 M HNO_3 (30 min), and deionized water (30 min), followed by drying at 60 °C. For the FeO_x/Ni catalyst, 1.685 g $NiSO_4 \cdot 7H_2O$ and 2.399 g $Fe_2(SO_4)_3$ were dissolved separately in 30 mL deionized water, and then 3 mL of the $Fe_2(SO_4)_3$ solution was mixed with 27 mL of the $NiSO_4 \cdot 7H_2O$ solution to prepare the electrodeposition electrolyte. Electrodeposition was conducted at -1.8 V vs. Ag/AgCl for 600 s under stirring at 500 rpm, using CP as the working electrode, a carbon rod as the counter electrode, and Ag/AgCl as the reference electrode. The resulting catalyst was rinsed with anhydrous ethanol and dried under vacuum at 70 °C. Ni and FeO_x catalysts were prepared under similar conditions by using only $NiSO_4 \cdot 7H_2O$ or $Fe_2(SO_4)_3$ as the electrolyte, with deposition time for FeO_x extended to 1 h. For post-synthetic Ag modification, the FeO_x/Ni catalyst was immersed in 1 mM $AgNO_3$ solution for 30 min, rinsed with deionized water, and dried at 70 °C under vacuum to yield FeO_x/Ni-Ag

Structural analysis

FeO_x/Ni, FeO_x, and Ni catalysts were prepared on CP through electrodeposition. The FeO_x/Ni-Ag

heterostructure was subsequently produced by immersing FeO_x/Ni in an Ag^+ solution to induce ion exchange. SEM images show that FeO_x/Ni maintains a similar morphology before and after ion exchange, exhibiting dendritic aggregates composed of nanoparticles (Supplementary Fig. 4a–f). FeO_x forms a relatively smooth surface coating (Supplementary Fig. 4g), whereas the Ni catalyst consists of sub-100 nm particles assembled into a branched architecture (Supplementary Fig. 4h,i). TEM analysis reveals that FeO_x/Ni-Ag contains abundant interfaces, and the corresponding SAED pattern exhibits diffraction rings characteristic of crystalline Ni (Supplementary Fig. 5a,b). HRTEM images further indicate that FeO_x/Ni-Ag comprises randomly distributed Ni nanocrystallites, Ag nanoparticles, and amorphous FeO_x domains (Supplementary Fig. 5c,d). The lattice fringes at the regions marked in Supplementary Fig. 5d correspond to d-spacings of 0.204 nm and 0.236 nm, assigned to the (111) planes of fcc Ni and fcc Ag, respectively (Supplementary Fig. 5e). In addition, the homogeneous distribution of Fe, Ni, and Ag at the sub-micrometer scale confirmed by TEM energy-dispersive X-ray spectroscopy (EDS) elemental mappings (Supplementary Fig. 5f). The phase composition and spatial distribution of FeO_x and Ni domains in FeO_x/Ni are similar to those in FeO_x/Ni-Ag (Supplementary Fig. 6). To resolve the structural states of the individual components, AC-HAADF-STEM imaging and the corresponding elemental maps reveal an intermixed distribution of amorphous FeO_x and Ni nanocrystals, with Ag nanoparticles uniformly decorating the FeO_x/Ni framework (Fig. 2c – e and Supplementary Fig. 7). XRD patterns of FeO_x/Ni-Ag and the control catalysts exhibit the diffraction peaks of fcc Ni, whereas no FeO_x peaks are detected due to its low crystallinity. The absence of Ag diffraction peaks indicates its low loading and nanoscale dispersion, consistent with the microscopy observations (Supplementary Fig. 8).

The electronic structures of FeO_x/Ni-Ag were probed by XAS and XPS. Fe *K*-edge XANES spectra of the catalysts and standards (Supplementary Fig. 9a) were used to establish an energy-oxidation state calibration based on the reference compounds, enabling determination of Fe valence states of 2.73, 2.75, and 2.94 for FeO_x/Ni-Ag, FeO_x/Ni, and FeO_x, respectively (Supplementary Fig. 9b). Ni *K*-edge XANES analysis yields corresponding Ni valences of 0.20, 0.20, and 0.04 for FeO_x/Ni-Ag, FeO_x/Ni, and the Ni catalyst, respectively (Supplementary Fig. 9d,e). The Ag *K*-edge XANES of FeO_x/Ni-Ag exhibits a negative shift relative to Ag foil (Supplementary Fig. 9g), indicating electron-rich Ag nanoparticles. These results show electron transfer from Ni to Fe upon formation of the FeO_x/Ni heterostructure, while the low Ag loading limits its impact on Fe and Ni valence states. EXAFS analysis further resolves the local coordination. Fe *K*-edge EXAFS (Supplementary Fig. 9c) shows dominant Fe-O (~1.53 Å) and Fe-Metal (M) (~2.20 Å) coordination for synthesized catalysts, while the characteristic Fe-Fe scattering at ~2.61 Å in crystalline Fe_2O_3 is absent, consistent with disordered FeO_x domains. Ni *K*-edge EXAFS spectra display only metallic Ni-M coordination at ~2.17 Å in FeO_x/Ni-Ag, FeO_x/Ni, and Ni catalyst (Supplementary Fig. 9f). Variations in the Fe-M and Ni-M peak intensities relative to the references support the presence of Fe-Ni coordination in

FeO_x/Ni-Ag. The Ag-M peak in the Ag *K*-edge EXAFS of FeO_x/Ni-Ag appears weakened and shifted to lower R compared with the Ag-Ag shell in Ag foil, reflecting the formation of shorter Ag-Fe/Ni bonds. (Supplementary Fig. 9h) WT analyses corroborate oxidized Fe with metallic Ni and Ag in FeO_x/Ni-Ag (Supplementary Fig. 10). Surface-sensitive XPS provides complementary evidence. The Fe $2p_{3/2}$ peaks of FeO_x/Ni shift by -0.3 eV relative to FeO_x (711.4 eV), consistent with electron shift from Ni to Fe (Supplementary Fig. 11c). Ni 2*p* spectra of catalysts display both Ni^{2+} and Ni^0 features, and the minimal variations in peak positions are likely dominated by surface oxidation incurred upon air exposure (Supplementary Fig. 11d). FeO_x/Ni-Ag shares the same elemental composition as FeO_x/Ni, except for the presence of metallic Ag nanoparticles (Supplementary Fig. 11e).

The composition of FeO_x/Ni-Ag was assessed by XPS, SEM-EDS, TEM-EDS, and inductively coupled plasma optical emission spectroscopy (ICP-OES), yielding Fe:Ni:Ag atomic ratios of 15.04:7.36:3.46, 31.28:17.42:1.25, 20.86:9.93:1.28, and 8.41:24.29:0.20, respectively (Supplementary Fig. 12 and Supplementary Table 2). The progressive decrease in Ag content with increasing probing depth indicates surface enrichment of Ag, suggesting enhanced noble-metal utilization. Meanwhile, the Fe:Ni ratio shifts from ~2:1 in surface-sensitive XPS/EDS to ~1:3 in bulk-sensitive ICP-OES, revealing a Ni-rich interior that is expected to improve electrical conductivity and facilitates FeO_x nucleation. Interfacial SEM-EDS mappings confirm this compositional gradient (Supplementary Fig. 13 a–d). Apart from the absence of Ag, FeO_x/Ni shows a comparable elemental distribution (Supplementary Fig. 13e,f).

Characterization

SEM images were acquired on a Zeiss GeminiSEM 300 equipped with an Oxford Xplore EDS detector. TEM, HRTEM, HAADF-STEM, SAED, and EDS mapping were performed on an FEI Tecnai G2 F20 using copper grids, while aberration-corrected STEM imaging was conducted on a Titan G2 80-200 Chemi STEM (FEI). XRD patterns were recorded on a Bruker D8 Advance diffractometer (Cu Kα, 40 kV, 40 mA). XPS measurements were carried out on an ESCALAB 250Xi with a monochromatic Al Kα source. XAS at the Fe, Ni, and Ag K-edges was collected at TLS 17A1 and TPS 44A beamline of NSRRC (Taiwan). Elemental compositions were determined by ICP-OES (Agilent 5110), and NMR spectra were obtained on a Bruker AV600. Online DEMS was performed with a QAS 100 system, SR-FTIR spectra on a Thermo Fisher Nicolet 6700 spectrometer at BL01B beamline of SSRF (Shanghai), and Raman spectra on a LabRAM HR-Evolution microscope using a 532 nm laser.

Electrochemical measurements

Electrochemical measurements were performed on a Corrtest CS310M workstation in a conventional H-type cell (50 mL per chamber). The cathode and anode compartments were separated by a Nafion 211 proton

exchange membrane. The Nafion 211 membrane (2 × 2 cm^2, 25.4 μm) was sequentially treated in 3 wt.% H_2O_2, 1 M H_2SO_4, and deionized water at 80 °C for 1 h, followed by rinsing with deionized water. Catalysts, an Hg/HgO electrode, and a platinum sheet electrode (1 × 2 cm^2) were used as the working, reference, and counter electrodes, respectively. The geometric area of the working electrode exposed to the electrolyte was 0.25 cm^2. The catalyst loading was determined to be ~8 mg cm^{-2} by calculating the mass difference before and after deposition. The catholyte and anolyte consisted of 1 M KOH plus 1 M KNO_3 and 1 M KOH, respectively, with a volume of 30 mL each. NO_3RR measurements were performed at a stirring rate of 600 rpm in a 25 °C water bath. All potentials (vs. Hg/HgO) were converted to RHE using the following equation (1):

$$E\,(\mathrm{vs.RHE}) = E\,(\mathrm{vs.Hg/HgO}) + 0.098 + 0.059\,\mathrm{pH} \quad (1)$$

LSV was carried out from 0.3 V to -0.7 V (vs. RHE) at a scan rate of 10 mV s^{-1}. Prior to LSV, the catalysts were conditioned potentiostatically at -0.5 V (vs. RHE) until a stable response was obtained. Chronoamperometry was performed at a constant potential for 1 h to quantify the reaction products. Following NO_3RR, the electrolyte was immediately stored at 2-6 °C to ensure that product analysis was completed within 72 h. For stability tests, the 45 mL electrolyte was refreshed every 12 h, and a 1 M HCl solution was used to capture volatilized NH_3. The electrochemical double-layer capacitance (C_{dl}) was determined by cyclic voltammetry (CV) at scan rates of 20, 40, 60, 80, and 100 mV s^{-1} within the non-Faradaic potential region. The ECSA was calculated using equation (2):

$$\mathrm{ECSA} = \frac{C_{dl}}{C_s} \quad (2)$$

Where a C_s of 40 μF cm^{-2} was employed. EIS was conducted over a frequency range of 0.1-10^4 Hz. HER and OER measurements were conducted using procedures analogous to those for NO_3RR, with 1 M KOH as the electrolyte and different applied potentials.

All reported data, including standard deviations, were derived from three independent experiments.

Calculation of the FE and yield rate

The FE was calculated using the following equation (3):

$$\mathrm{FE} = \frac{n \times c \times V \times F}{Q} \times 100\ (\%) \quad (3)$$

Where n denotes the number of electrons transferred in the reaction (8 for $NO_3^- \rightarrow NH_3$ and 2 for $NO_3^- \rightarrow NO_2^-$), F is the Faraday constant (96,485 C mol^{-1}), c (mol L^{-1}) is the product concentration, V (L) is the electrolyte volume, and Q (C) is the total charge passed during electrolysis.

The yield rate was determined according to the following equation (4):

$$Y = \frac{c \times V \times M}{t \times s} \ (\mathrm{mg\ h^{-1}\ cm^{-2}}) \quad (4)$$

Where c (mol L^{-1}) is the product concentration, V (L) is the electrolyte volume, M (g mol^{-1}) is the molar mass of the product, t (h) is the electrolysis time, and s (cm^2) is the geometric area of the electrode.

Colorimetric quantification of NH_3

The indophenol blue method was used to quantify NH_3 concentrations. Three aqueous solutions were prepared as follows: (a) 1 M KOH containing 5 wt% sodium citrate and 5 wt% salicylic acid, (b) 0.05 M NaClO, and (c) 1 wt% sodium nitroferricyanide. A defined volume of electrolyte was diluted to 2 mL with deionized water, followed by the addition of 2 mL of solution (a), 1 mL of solution (b), and 0.2 mL of solution (c). The mixture was maintained at room temperature (25 °C) for 2 h and analyzed by UV-vis spectroscopy. NH_3 concentrations were determined from the absorbance at ~655 nm, with a calibration curve constructed using standard NH_4Cl solutions.

Determination of NH_3 by NMR

Quantitative ^1H NMR (600 MHz) analysis of NH_3 was carried out in DMSO-d_6 with maleic acid as the internal standard. Calibration curves were constructed from standard mixtures containing NH_4Cl solution (0.5 mL), 20 mM maleic acid (0.5 mL), 0.8 M H_2SO_4 (0.5 mL), and deionized water (0.2 mL); 0.5 mL of each mixture was diluted with 0.5 mL DMSO-d_6 for measurement. The integrated peak-area ratio of NH_4^+ to maleic acid was used for quantification. For NO_3RR tests, electrolysis was performed at -0.4 V in 1 M KNO_3 + 1 M KOH for 1 h. A volume of 0.5 mL of the electrolyte was mixed with the reagents described above and analyzed by NMR to determine the NH_4^+ concentration.

^{15}N isotope-labeling experiments were conducted to trace NH_3 formation during NO_3RR, with $^{14}NH_4^+$ and $^{15}NH_4^+$ quantified by ^1H NMR (600 MHz); $K^{14}NO_3$ and $K^{15}NO_3$ were used as nitrogen sources, and test solutions were prepared as for NH_3 calibration but with 0.1 M NO_3^- in the electrolyte.

Colorimetric calibration of NO_2^-

NO_2^- concentrations were measured via the Griess method. The chromogenic reagent, prepared by dissolving 0.4 g p-dimethylaminobenzaldehyde and 0.02 g N-(1-naphthyl) ethylenediamine dihydrochloride in 5 mL ultrapure water and 1 mL phosphoric acid (ρ = 1.70 g mL^{-1}), was added (0.1 mL) to 5 mL of diluted electrolyte. After 20 min, UV-vis absorbance was recorded, and NO_2^- concentrations were determined at ~540 nm using a NO_2^- calibration curve. $NaNO_2$ powder was pre-dried in a vacuum oven at 90 °C for 8 h before preparing standard NO_2^- solutions.

Electrochemical *In-situ* Raman spectroscopy

In-situ Raman spectroscopy was performed in a custom three-electrode electrolytic cell. (Supplementary Fig 41a) Prior to reaction, an initial Raman spectrum was collected to characterize the pristine state of the catalysts. The catalyst was then activated to a stable state via CV. *In-situ* measurements were conducted under chronoamperometry once the current stabilized, over a potential range of 0.2 to -0.5 V (vs. RHE) with 100 mV intervals.

Operando XAS measurements

Operando XAS at the Fe, Ni, and Ag K-edges was performed at the Taiwan Photon Source (TPS) 44A quick-scanning beamline using a custom *operando* XAS setup. (Supplementary Fig 39b) An initial spectrum was collected after the setup assembly. The catalyst was then activated to a stable state at -0.3 V (vs. RHE). Subsequent *operando* measurements were conducted using chronoamperometry over 0.2 to -0.5 V (vs. RHE) with 100 mV intervals. XAS spectra were recorded once the current reached a stable value at applied potentials. (Supplementary Fig. 41b)

Electrochemical *In-situ* SR-FTIR Measurements

In-situ SR-FTIR measurements were carried out in an electrolytic cell using 1 M KOH plus 1 M KNO_3 as the electrolyte under potentiostatic control for the synthesized catalysts at the BL01B beamline of SSRF. (Supplementary Fig 39c) Spectra were recorded from 0.2 V to -0.5V (vs. RHE) at 100 mV intervals. A background spectrum collected at 0.4 V vs. RHE was used to normalize all subsequent spectra. The catalyst was first activated to a stable state via CV before performing *in-situ* SR-FTIR measurements. (Supplementary Fig. 41c)

Online DEMS Analysis

Online DEMS measurements were performed using a mass spectrometer coupled with an electrochemical workstation (Linglu QAS100). FeO_x/Ni-Ag served as the working electrode, a platinum wire as the counter electrode, and Ag/AgCl as the reference electrode. The electrolyte consisted of 1.0 M KOH with 1 M KNO_3. LSV was carried out from 0.2 to -0.5 V (vs. RHE), and mass signals were recorded during a single scan.

MEA Performance Testing

A two-electrode system was assembled using nickel foam (1 cm^2, 0.5 mm) coated with FeO_x/Ni-Ag as both cathode and anode. The anion-exchange membrane (AM01-110, 2 × 2 cm^2, 110 μm, KMem) was pretreated by immersion in a 1 M KOH + 1 M KNO_3 solution for 12 h. Both catholyte and anolyte comprised 1 M KOH with 1 M KNO_3 and were circulated through the chambers using a peristaltic pump (Kamoer KXP100-GB) at 20 mL min^{-1}. To minimize the effects of KNO_3 depletion and electrolyte pH changes on device

performance, the electrolytes were replaced regularly. A 1 M HCl solution was used to capture potentially volatilized NH_3 and prevent its loss. All measurements were performed at 25 °C. (Supplementary Fig. 41d)

Computational methods

DFT Calculations

All first-principles calculations were conducted using spin-polarized density functional theory (DFT) within the Vienna Ab initio Simulation Package (VASP)[1,2]. The projector augmented wave (PAW) pseudopotentials were utilized in conjunction with the Perdew-Burke-Ernzerhof (PBE) functional under the generalized gradient approximation (GGA)[3-6]. The convergence thresholds for energy and atomic forces were fixed at 10^{-5} eV and 0.01 eV $Å^{-1}$, respectively. For the decoupling of interlayer interactions under periodic boundary conditions, a vacuum layer of 20 Å was inserted perpendicular to the layers. Following comprehensive energy convergence tests, a plane-wave cutoff energy of 500 eV was chosen, and Brillouin zone sampling was performed using a 4 × 1 × 1 Monkhorst-Pack k-point mesh[7]. In order to account for van der Waals (vdW) interactions between reaction intermediates and catalysts, the DFT-D3 method within the Grimme scheme was included[8]. Furthermore, a polarizable implicit solvent model was implemented via the VASPsol module, with the dielectric constant set to 78.4 to simulate an aqueous environment[9]. The charge transfer between the substrate and the adsorbates was quantified using Bader charge analysis[10,11]. Meanwhile, the crystal orbital Hamilton populations (COHP) were derived from the DFT wavefunctions using LOBSTER[12,13]. Finally, to directly evaluate the thermodynamic stability of the catalyst structure, ab initio molecular dynamics (AIMD) simulations, including constraint-preserving AIMD (cp-AIMD), were performed[14,15]. These simulations employed a slow-growth methodology within the canonical (NVT) ensemble, utilizing a Nosé-Hoover thermostat maintained at 300 K.

The Gibbs free energy changes (ΔG) calculation

Following the chemical framework of Nørskov et al.[16], the Gibbs free energy is systematically evaluated using the computational methods detailed below. The reaction pathway in alkaline media comprises the following elementary steps[17]:

$$^{*}NO_3 + 0.5H_2 = {}^{*}NO_3H$$

$$^{*}NO_3H + 0.5H_2 = {}^{*}NO_2 + H_2O$$

$$^{*}NO_2 + 0.5H_2 = {}^{*}NO_2H$$

$$^{*}NO_2H + 0.5H_2 = {}^{*}NO + H_2O$$

$$^{*}NO + 0.5H_2 = {}^{*}NOH$$

$$^{*}NOH + 0.5H_2 = {}^{*}NHOH$$

$$^{*}NHOH + 0.5H_2 = {}^{*}NH_2OH$$

$$^{*}NH_2OH + 0.5H_2 = {}^{*}NH_2+H_2O$$

$$^{*}NH_2 + 0.5H_2 = {}^{*}NH_3$$

where * denotes an adsorption site. The Gibbs free energy change (ΔG) of the multistep NO_3RR process is calculated as:

$$\Delta G = \Delta E + \Delta ZPE - T\Delta S + \Delta G\mathrm{U} + \Delta G_{\mathrm{pH}} \quad (5)$$

where ΔE is the electronic energy difference from DFT calculations, ΔZPE is the zero-point energy correction, T is the temperature (298.15 K), and ΔS is the entropy change. The contribution from the applied electrode potential U is given by $\Delta GU = -eU$. For the calculation, the pH-dependent term is $\Delta G_{pH} = k_B T \ln(10) \times pH$, where k_B is the Boltzmann constant and the pH is set to 14.

Machine learning prediction

To identify the optimal structural configuration, we developed a machine learning pipeline that integrates data collection, feature engineering, model training, and validation. This approach deciphered the structure-property relationships between the catalytic performance and key computational descriptors of the reaction sites, with correlation analysis further quantified using Pearson coefficients[18]. All modeling was implemented using the Scikit-learn library in Python 3 [19], with the complete dataset and preprocessing details provided in the Supporting Information. Here, we employed six machine learning algorithms for regression: Gradient-Boosting regression (GBR)[20], Random Forest (RF)[21], K-Nearest Neighbors (KNN)[22], Multilayer Perceptron (MLP)[23], Decision Tree (DT)[24]. The performance of these models is evaluated primarily through the widely accepted regression metrics R^2 (coefficient of determination), and RMSE (root mean square error).

$$R^2 = 1 - \frac{\sum_i (y_i - \hat{y}_i)^2}{\sum_i (y_i - \bar{y}_i)^2} \quad (6)$$

$$RMSE = \sqrt{\frac{1}{n}\sum_{i=1}^{n} (y_i - \hat{y}_i)^2} \quad (7)$$

where y_i corresponds to the DFT-calculated result, $\hat{y}_i$ signifies the value predicted by the machine learning model, $\bar{y}_i$ denotes the mean of all DFT values, and n indicates the number of observations considered. A robust regression performance is characterized by error metrics, such as RMSE, approaching zero and an R^2 value close to unity.

SISSO

The propensity of various noble metals to facilitate the formation of interfacial aqueous layers characterized by a strong hydrogen-bond network was investigated using the SISSO (Sure Independence Screening and Sparsifying Operator) method for descriptor identification[25,26]. The SISSO method, a machine learning technique with excellent screening capability in high-dimensional feature spaces, enables the effective extraction of key factors influencing material properties (e.g., catalytic activity) from complex data, thereby drastically reducing traditional trial-and-error costs while operating synergistically with the complementary machine learning approaches used in this work.

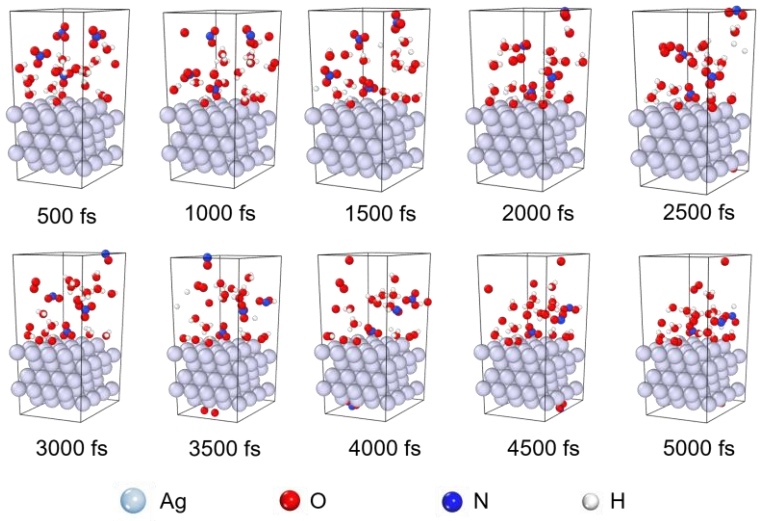

Supplementary Fig. 1 Evolution of H_2O and NO_3^- adsorption configurations on Ag nanoparticles as a function of time.

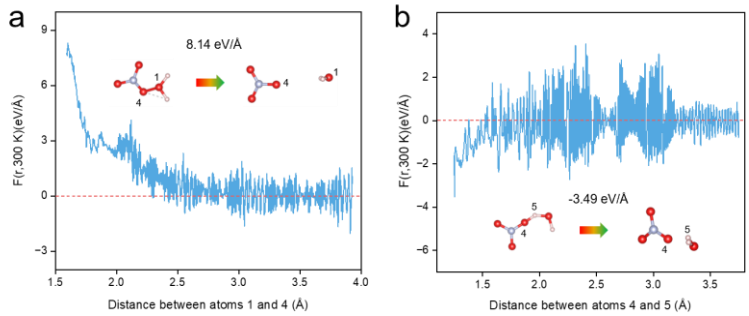

Supplementary Fig. 2 Ab initio molecular dynamics (AIMD) models of H_2O and NO_3^- adsorption on Ag nanoparticles at 5,000 fs, showing (a) $O(NO_3^-)$-$O(H_2O)$ and (b) $O(NO_3^-)$-$H(H_2O)$ interaction forces.

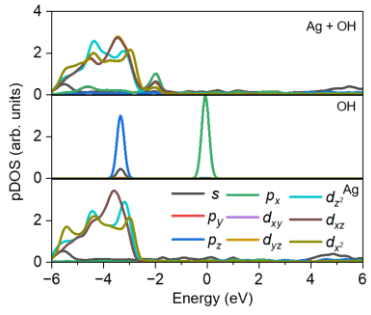

Supplementary Fig. 3 The pDOS of OH adsorbed on the Ag nanoparticle surface.

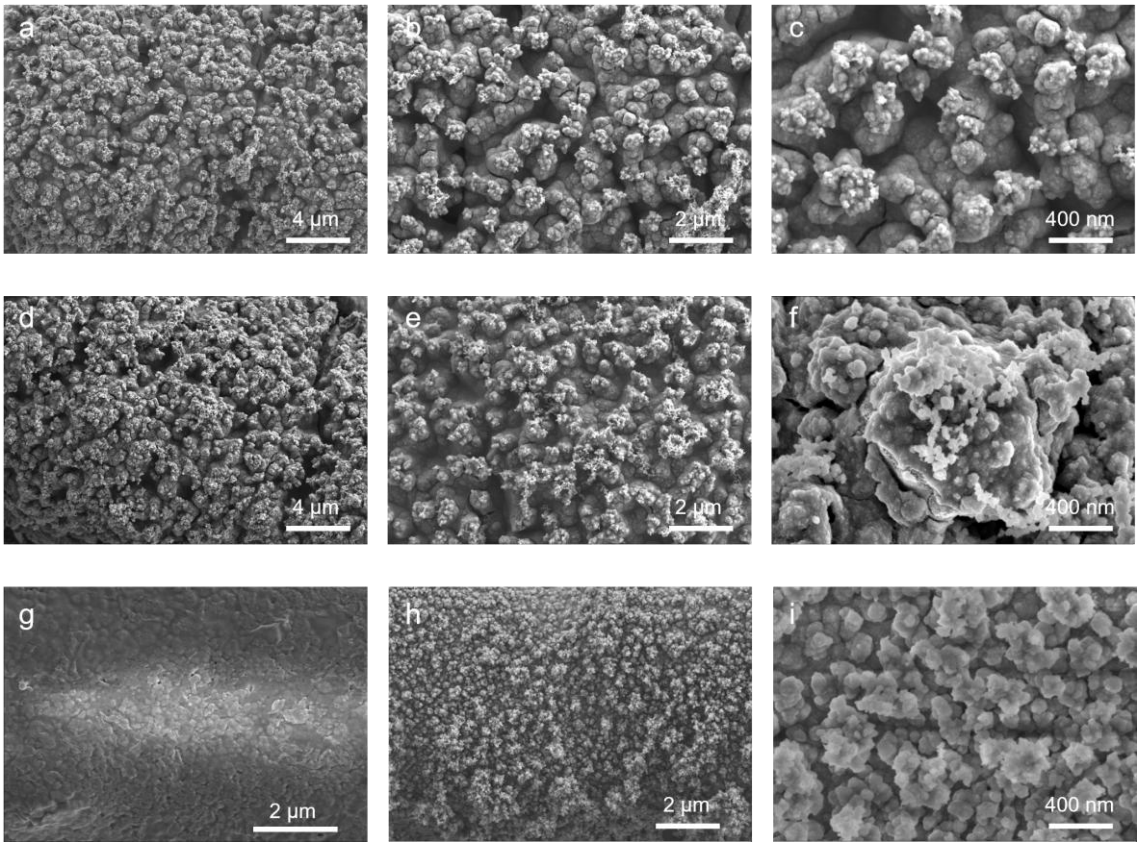

Supplementary Fig. 4 SEM images of (a-c) FeO_x/Ni-Ag, (d-f) FeO_x/Ni, (g) FeO_x, and (h,i) Ni catalysts.

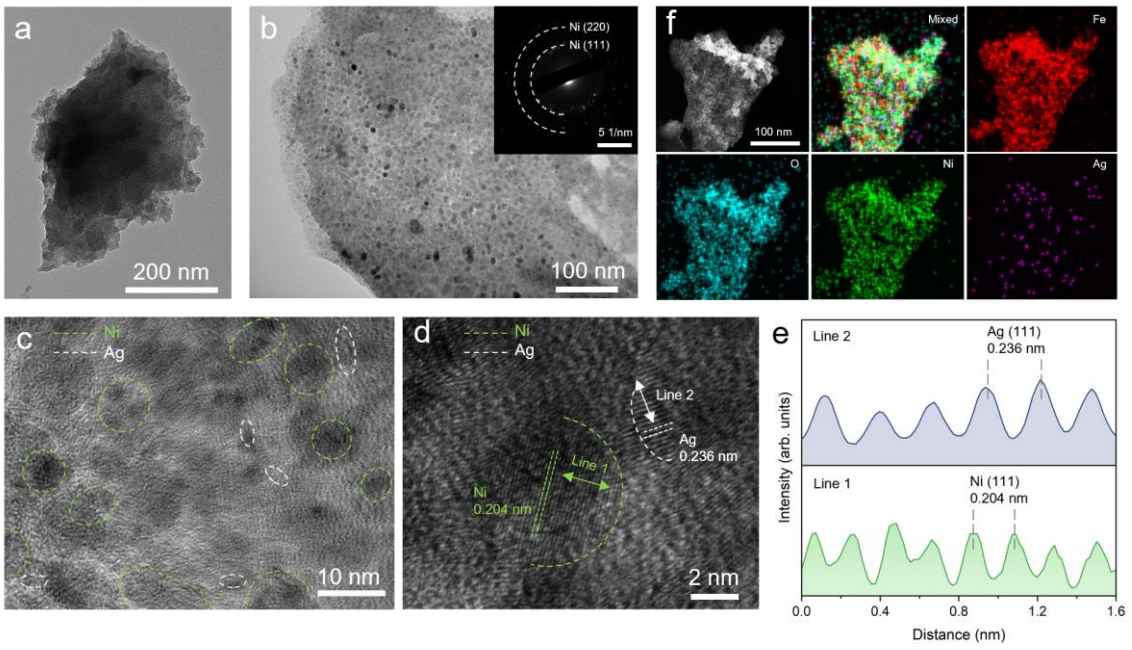

Supplementary Fig. 5 (a,b) TEM images of FeO_x/Ni-Ag, where the inset in (b) showing the corresponding SAED pattern. (c,d) HRTEM images of FeO_x/Ni-Ag. (e) Line profiles extracted from the regions indicated by arrows in (d), revealing the corresponding interplanar spacings. (f) TEM-EDS elemental mapping of FeO_x/Ni-Ag.

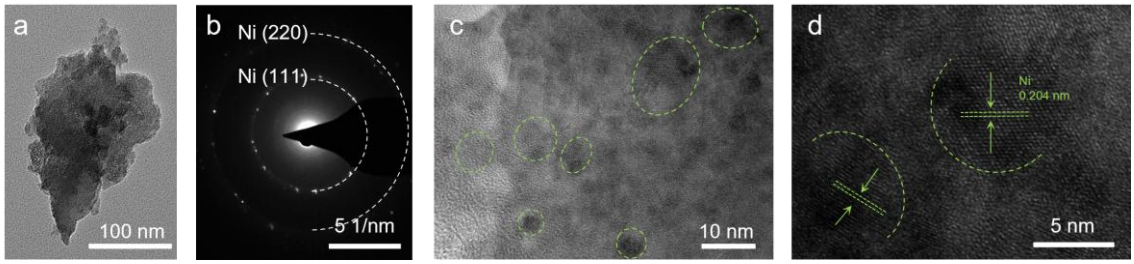

Supplementary Fig. 6 (a) TEM image, (b) SAED pattern, and (c,d) HRTEM images of FeO_x/Ni.

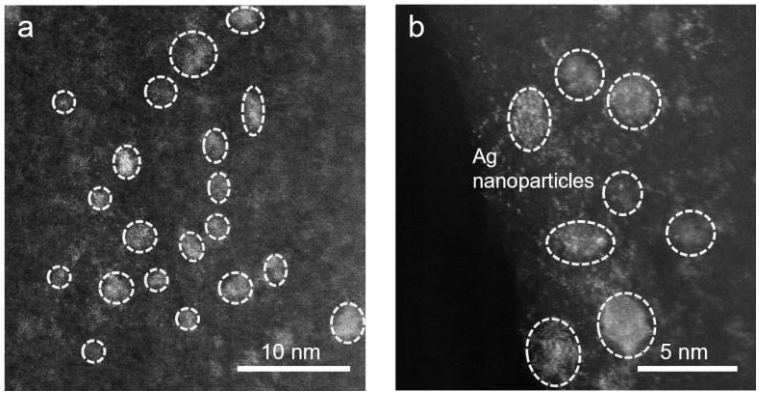

Supplementary Fig. 7 AC-HAADF-STEM images of FeO_x/Ni-Ag.

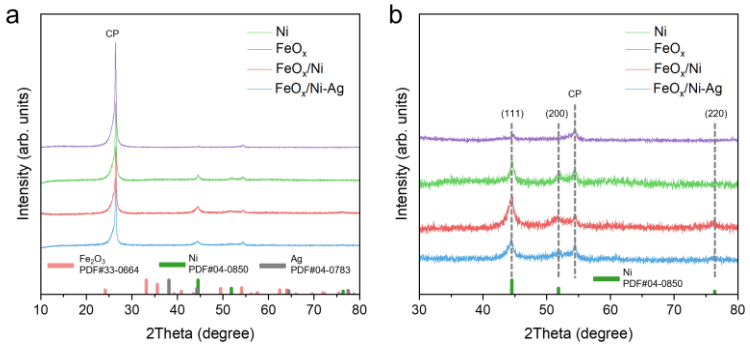

Supplementary Fig. 8 (a) XRD patterns of the FeO_x/Ni-Ag, FeO_x/Ni, FeO_x, and Ni catalysts. (b) Enlarged view of the XRD patterns.

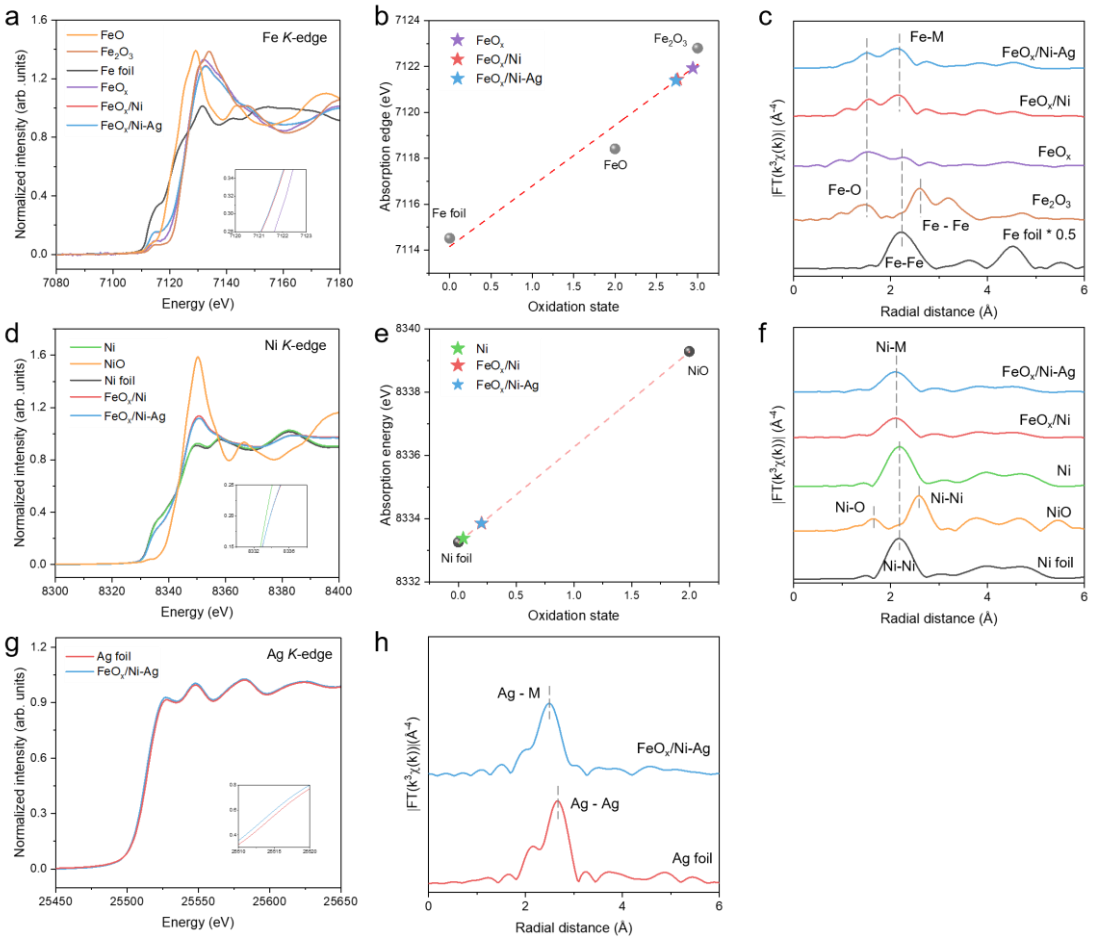

Supplementary Fig. 9 (a) Fe *K*-edge XANES spectra, (b) corresponding oxidation-state comparison derived from XANES fitting, and (c) Fe *K*-edge EXAFS spectra of the catalysts and reference samples. (d) Ni *K*-edge XANES spectra, (e) corresponding oxidation-state comparison derived from XANES fitting, and (f) Ni *K*-edge EXAFS spectra of the synthesized catalysts and Ni reference samples. (g) Ag *K*-edge XANES spectra, and (h) EXAFS spectra of FeO_x/Ni-Ag in comparison with Ag foil.

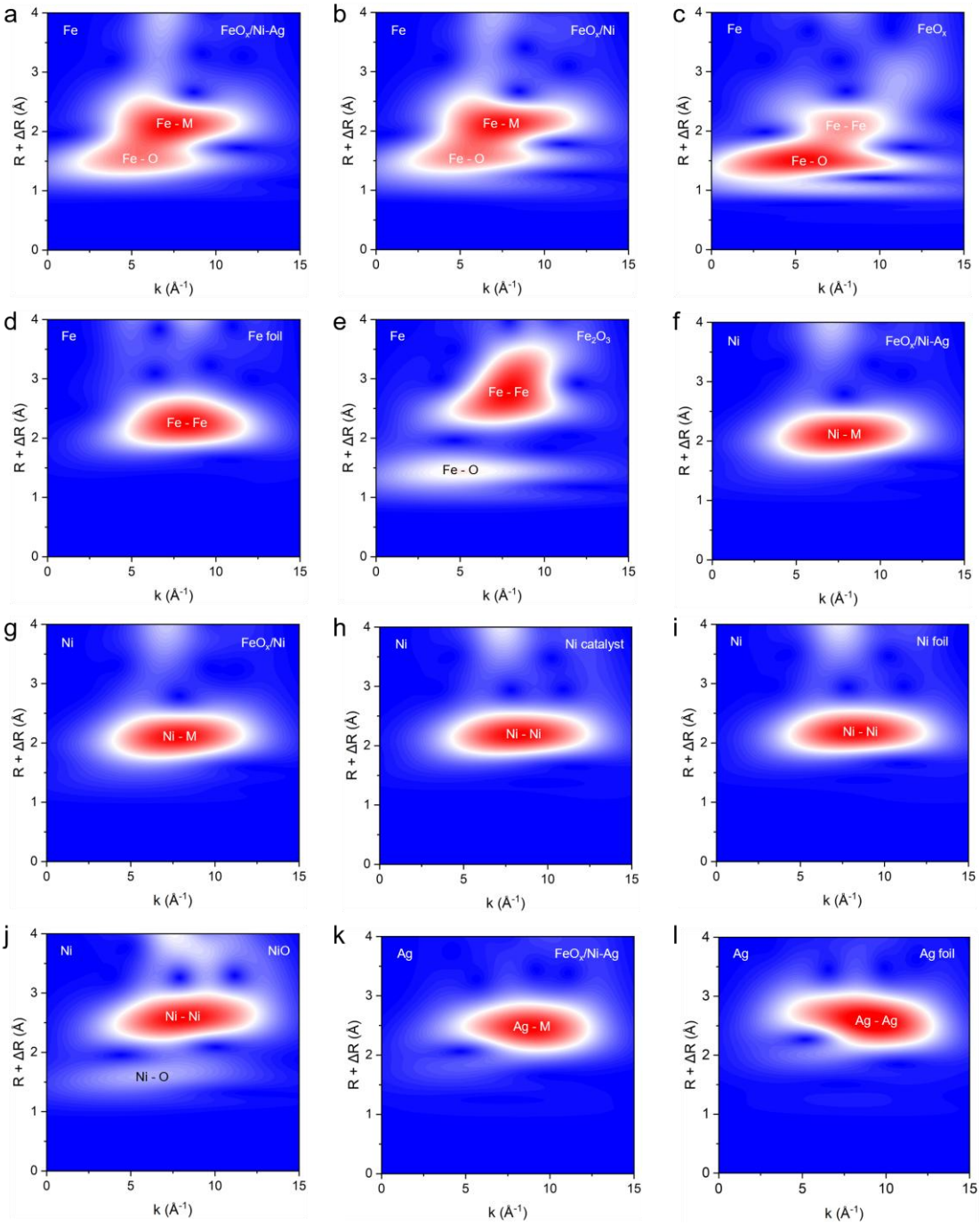

Supplementary Fig. 10 k^3-weighted EXAFS WT maps at the Fe, Ni, and Ag *K*-edges. (a-e) Fe *K*-edge WT plots for FeO_x/Ni-Ag, FeO_x/Ni, and FeO_x catalysts, as well as Fe foil and Fe_2O_3 references. (f-j) Ni *K*-edge WT plots for FeO_x/Ni-Ag, FeO_x/Ni, and Ni catalysts, as well as Ni foil and NiO references (i,j). (k,l) Ag *K*-edge WT plot for FeO_x/Ni-Ag catalyst, and Ag foil reference.

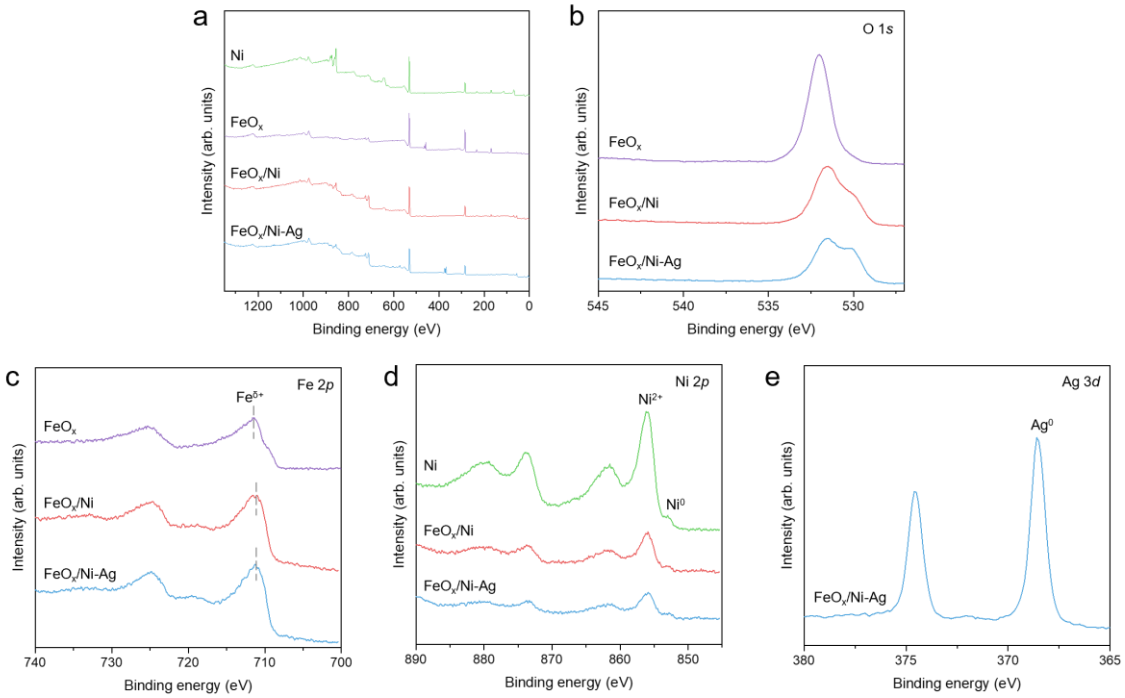

Supplementary Fig. 11 XPS characterization of the catalysts. (a) Survey spectra. High-resolution spectra of (b) O 1*s* and (c) Fe 2*p* for FeO_x/Ni-Ag, FeO_x/Ni, and FeO_x. (d) High-resolution spectra of Ni 2*p* for FeO_x/Ni-Ag, FeO_x/Ni, and Ni catalysts. (e) High-resolution Ag 3*d* spectrum for FeO_x/Ni-Ag.

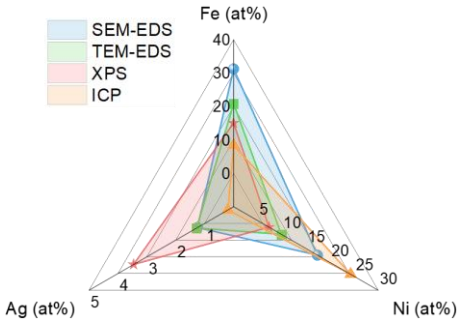

Supplementary Fig. 12 Atomic composition of FeO_x/Ni-Ag determined by SEM-EDS (corresponding to Supplementary Fig. 12a), TEM-EDS (Supplementary Fig. 5f), XPS (Supplementary Fig. 10), and ICP-OES analysis (Supplementary Table 2).

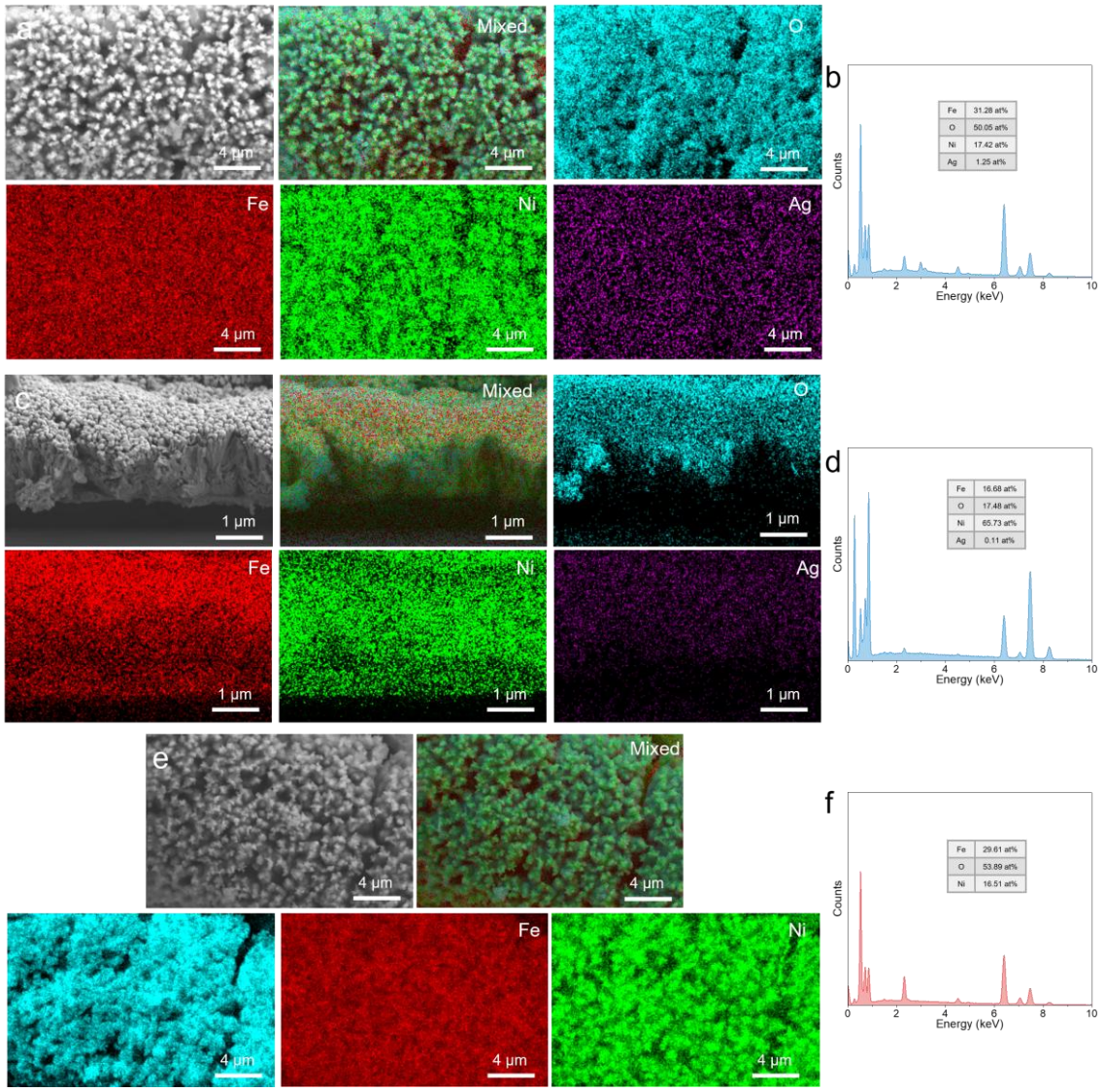

Supplementary Fig. 13 SEM-EDS elemental mapping of (a) FeO_x/Ni-Ag, (c) cross-sectional FeO_x/Ni-Ag, and (e) FeO_x/Ni, and the corresponding elemental spectra are presented in (b), (d), and (f), respectively.

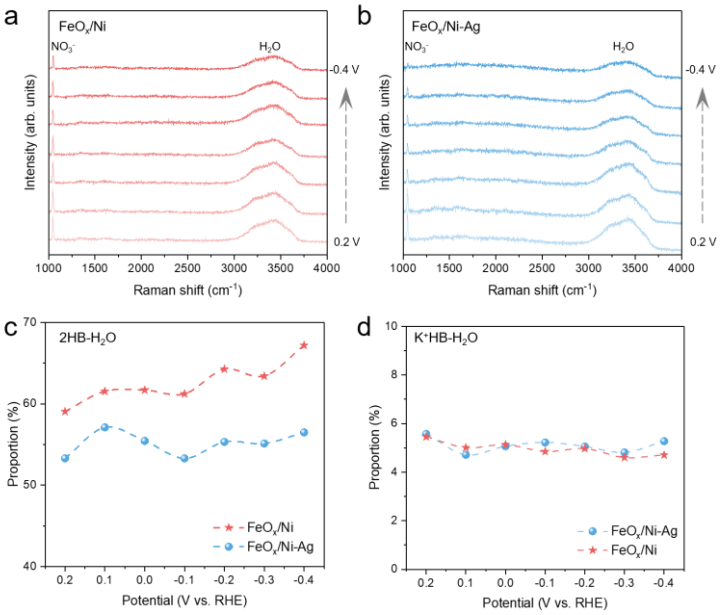

Supplementary Fig. 14 (a,b) *In-situ* Raman spectra of FeO_x/Ni-Ag and FeO_x/Ni during NO_3RR. (c,d) Comparison of interfacial water species ratios extracted from Raman analysis for FeO_x/Ni-Ag and FeO_x/Ni.

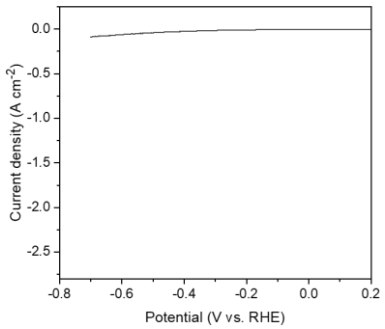

Supplementary Fig. 15 LSV curve of CP during NO_3RR.

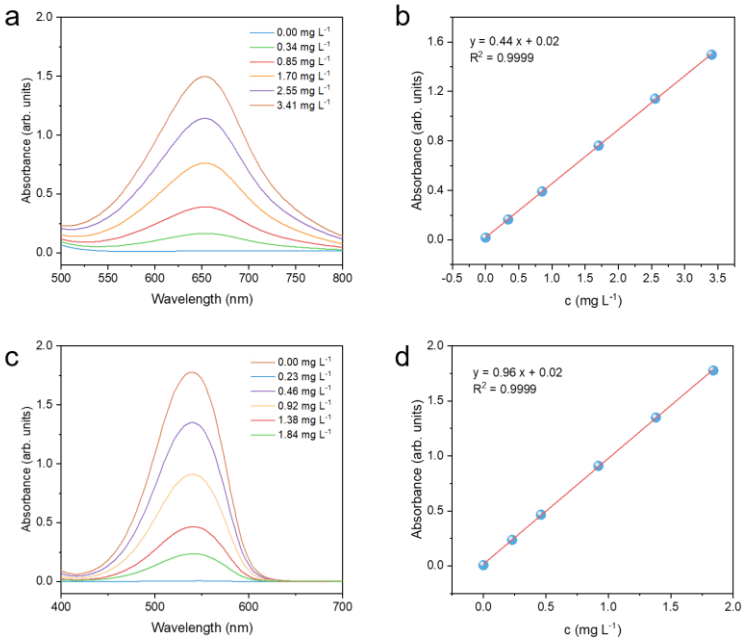

Supplementary Fig. 16 (a) UV-vis spectra and (b) calibration curves of standard solutions for NH_3 quantification using colorimetric analysis. (c) UV-vis spectra and (d) calibration curves of standard solutions for NO_2^- quantification.

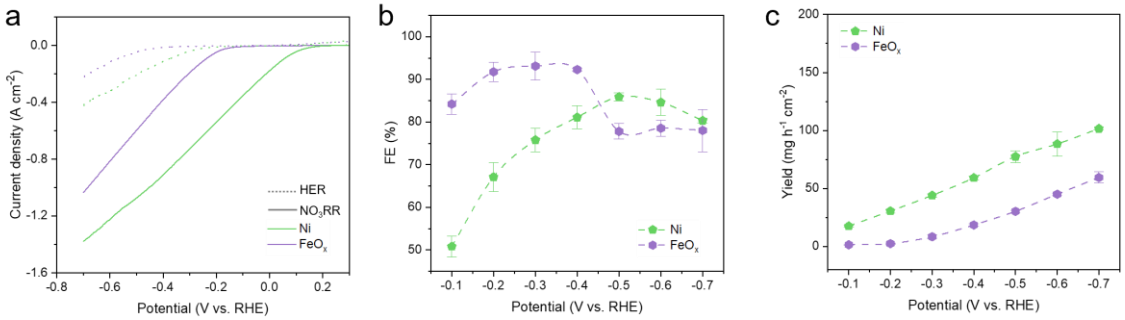

Supplementary Fig. 17 NO_3RR performance of FeO_x and Ni catalysts: (a) LSV curves; (b) FE of NH_3 at various applied potentials; (c) Comparison of NH_3 yield rates under corresponding potentials.

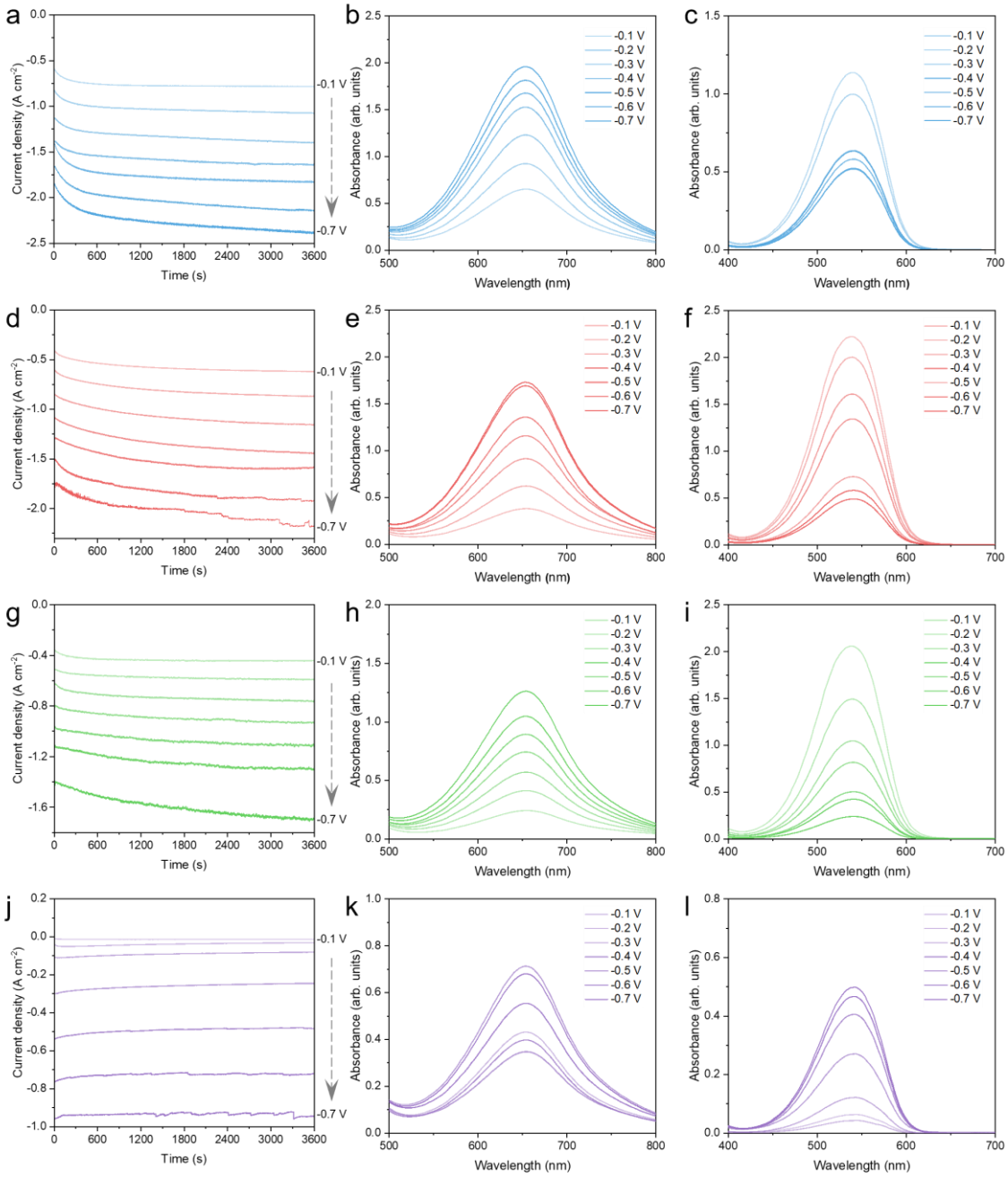

Supplementary Fig. 18 Data used for calculating NH_3 FE and yield. (a) I-t curves, (b) UV-vis absorption spectra of NH_3, and (c) UV-vis absorption spectra of NO_2^- for FeO_x/Ni-Ag. (d) I-t curves, (e) UV-vis absorption spectra of NH_3, and (f) UV-vis absorption spectra of NO_2^- for FeO_x/Ni. (g) I-t curves, (h) UV-vis absorption spectra of NH_3 absorption spectrum, and (i) UV-vis absorption spectra of NO_2^- for FeO_x. (j) I-t curves, (k) UV-vis absorption spectra of NH_3, and (l) UV-vis absorption spectra of NO_2^- for Ni catalyst.

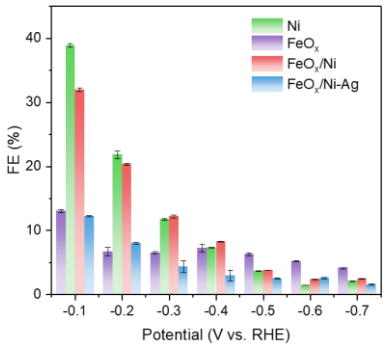

Supplementary Fig. 19 FE of NO_2^- for the synthesized catalysts at different applied potentials.

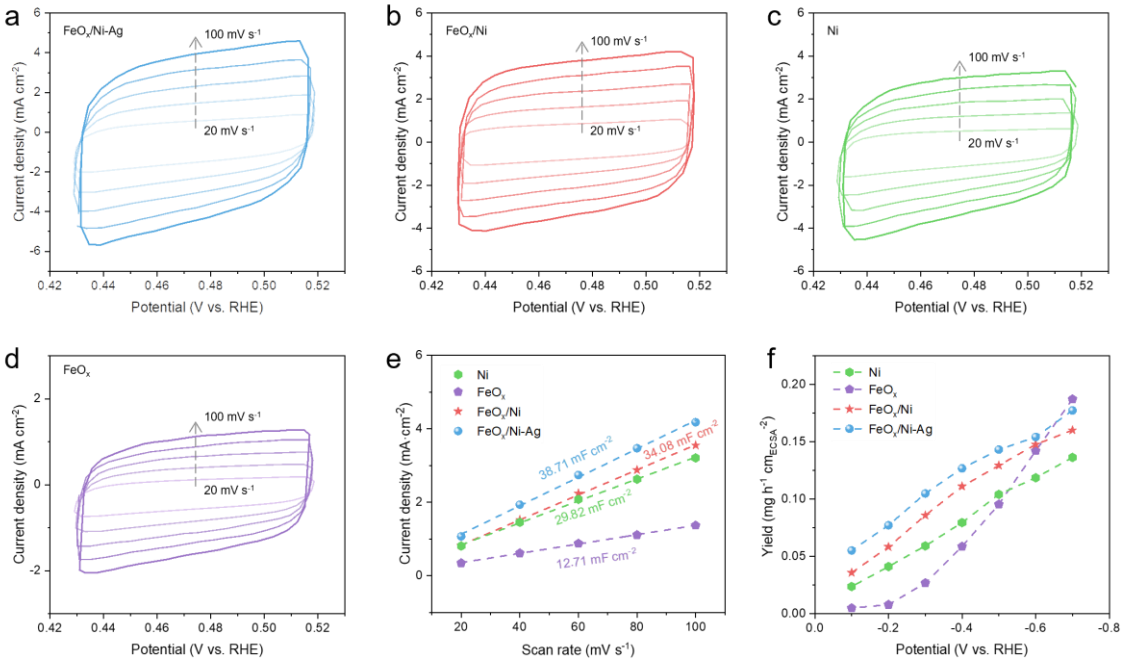

Supplementary Fig. 20 CV measurements for NO_3RR at different scan rates for (a) FeO_x/Ni-Ag, (b) FeO_x/Ni, (c) Ni, and (d) FeO_x catalysts. (e) Linear relationship between current density difference and scan rate. (f) NH_3 yield rates normalized to ECSA at different applied potentials.

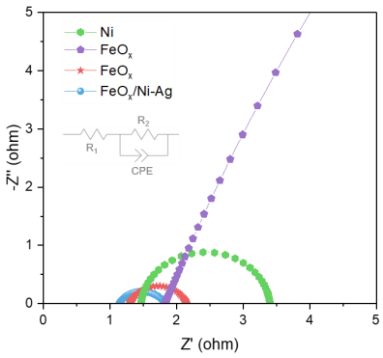

Supplementary Fig. 21 EIS fitting curves of FeO_x/Ni-Ag, FeO_x/Ni, FeO_x, and Ni catalysts.

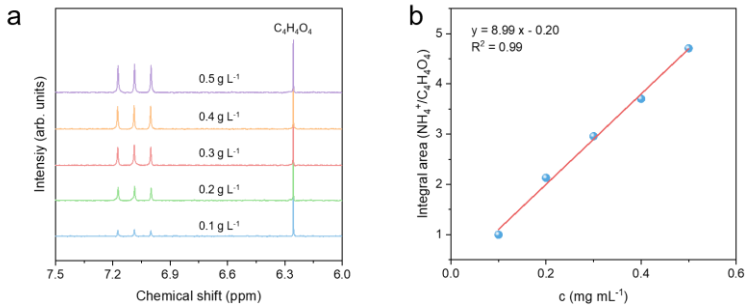

Supplementary Fig. 22 (a) ^{1}H NMR spectra of standard NH_3 solutions with varying concentrations and (b) the corresponding calibration curve.

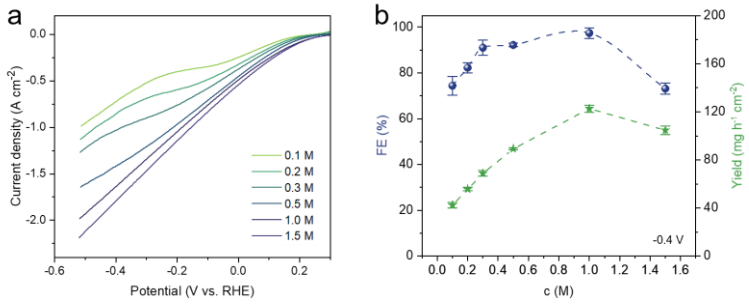

Supplementary Fig. 23 NO_3RR performance of FeO_x/Ni-Ag under varying NO_3^- concentrations. (a) LSV curves. (b) NH_3 FE and yield rate at -0.4 V (vs. RHE).

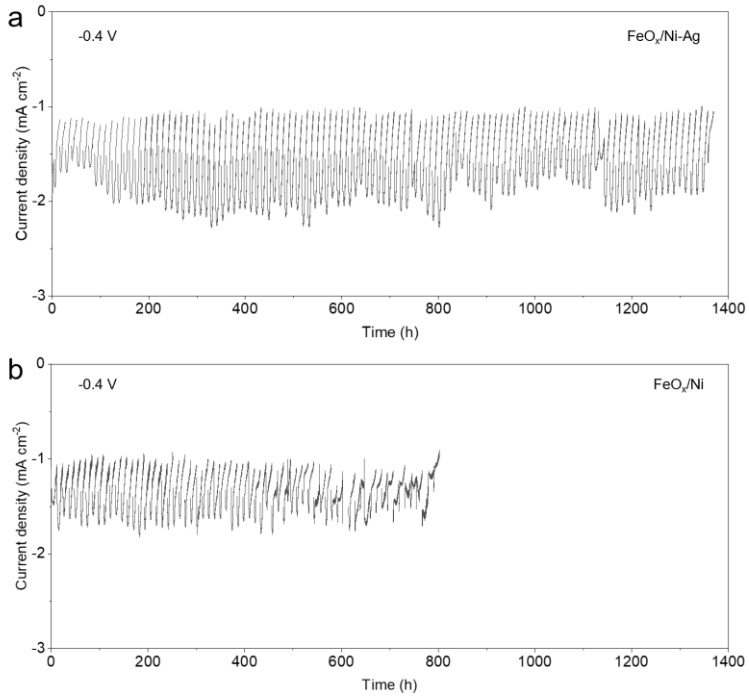

Supplementary Fig. 24 I-t curves of (a) FeO_x/Ni-Ag and (b) FeO_x/Ni during NO_3RR stability tests at -0.4 V (vs. RHE).

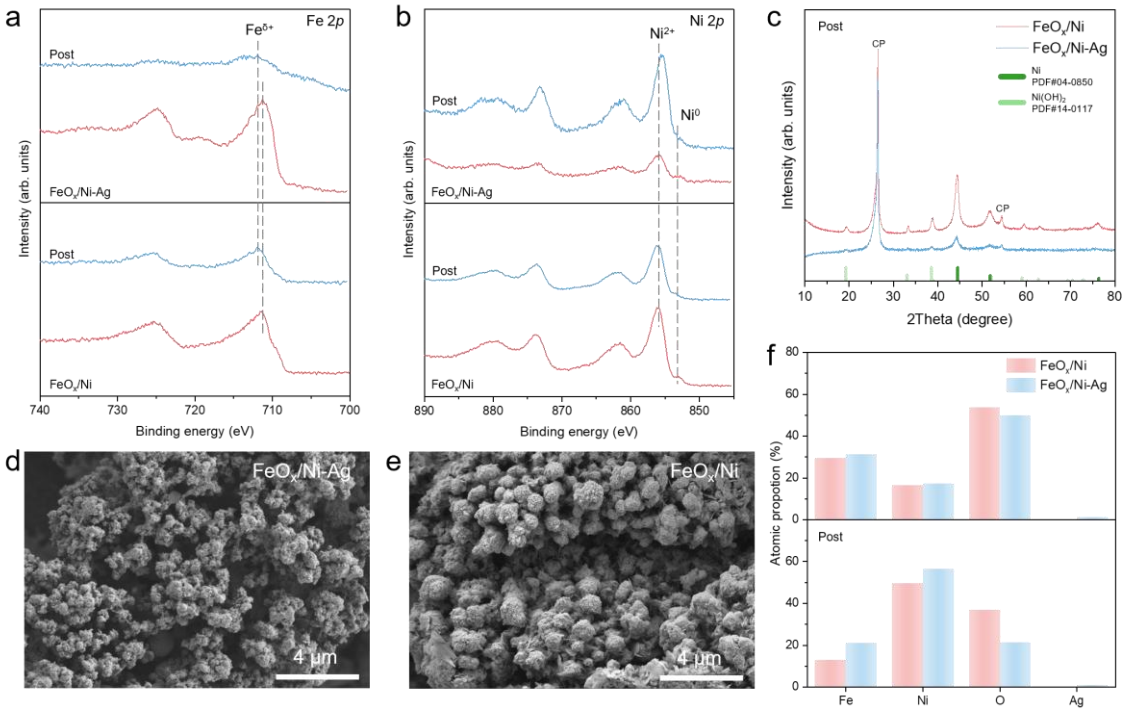

Supplementary Fig. 25 Post-mortem characterization after three-electrode NO_3RR stability tests. a,b, High-resolution Fe 2*p* (a) and Ni 2*p* (b) XPS spectra of FeO_x/Ni-Ag and FeO_x/Ni recorded before and after NO_3RR operation. c, XRD patterns of FeO_x/Ni-Ag and FeO_x/Ni after stability tests. d,e, SEM images of FeO_x/Ni-Ag (d) and FeO_x/Ni (e) after prolonged NO_3RR operation. f, Comparison of elemental compositions determined by SEM-EDS before and after stability tests for FeO_x/Ni-Ag and FeO_x/Ni.

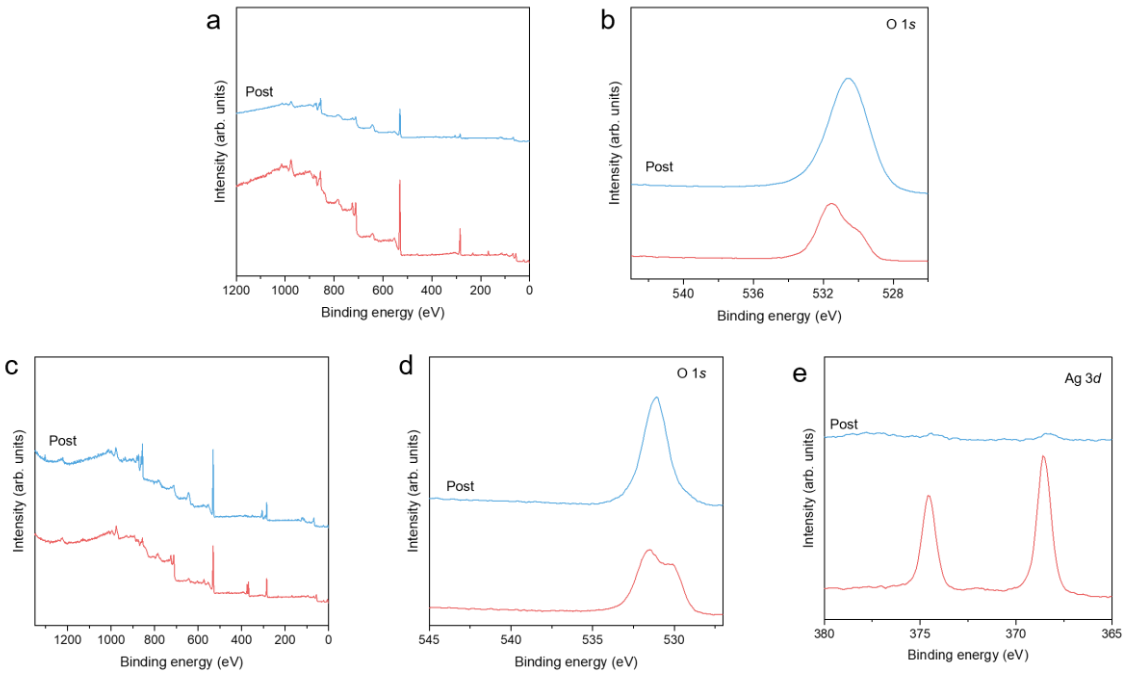

Supplementary Fig. 26 XPS comparison of catalysts before and after stability tests at -0.4 V. For FeO_x/Ni: (a) survey spectra, and (b) O 1*s* high-resolution spectra. For FeO_x/Ni-Ag: (c) survey spectra, (d) O 1*s* and (e) Ag 3*d* high-resolution spectra.

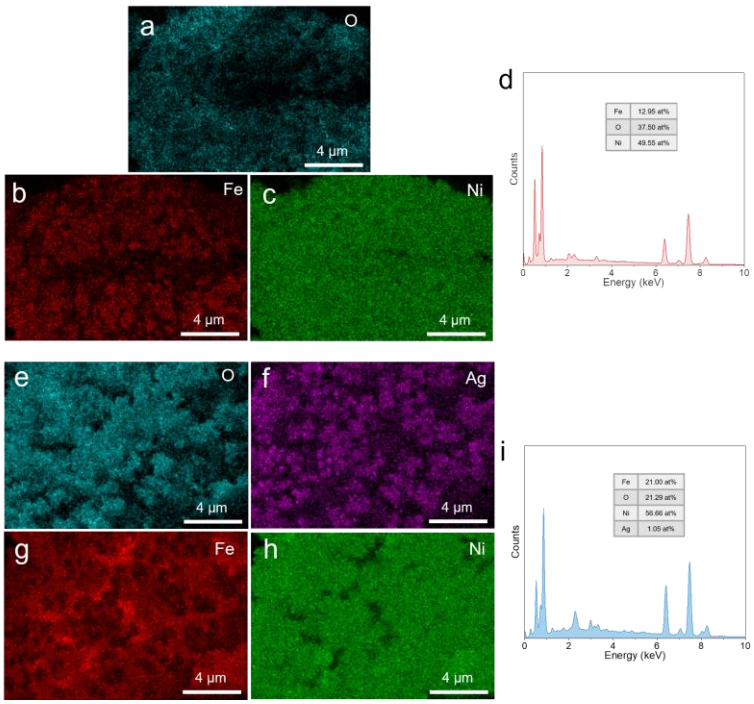

Supplementary Fig. 27 Post-stability characterization of catalysts in a three-electrode system. For FeO_x/Ni: (a-c) SEM-EDS elemental mappings, and (d) elemental composition spectrum. For FeO_x/Ni-Ag: (e-h) SEM-EDS elemental mappings, and (i) elemental composition spectrum.

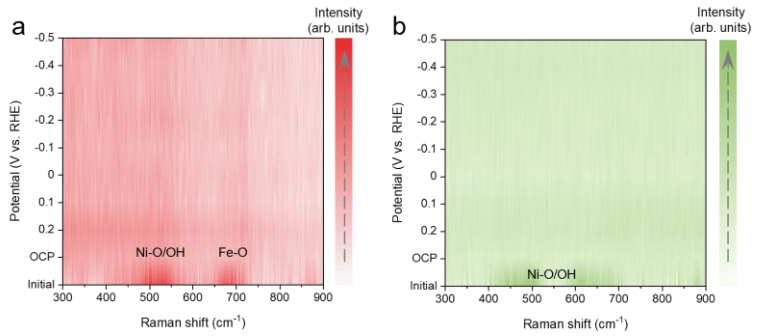

Supplementary Fig. 28 *In-situ* Raman spectra of (a) FeO_x/Ni and (b) Ni catalysts recorded at different applied potentials during NO_3RR.

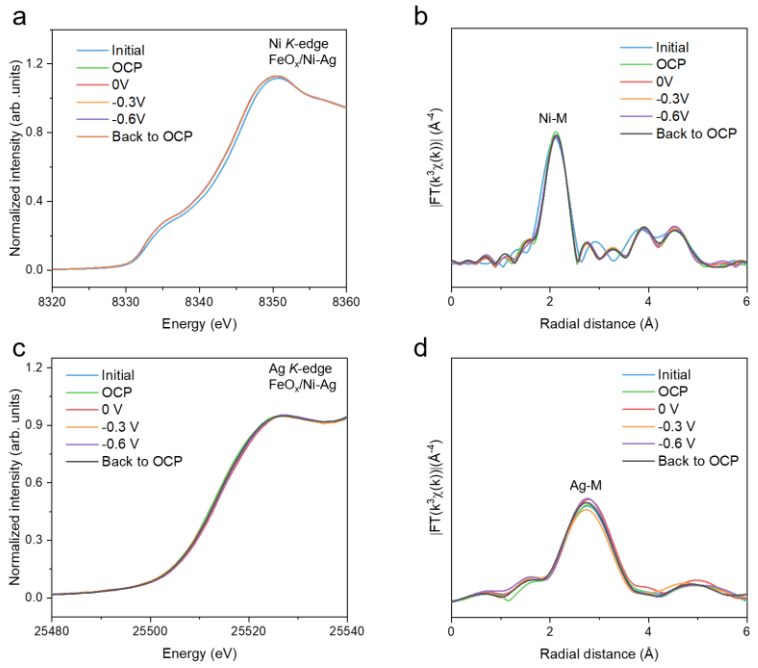

Supplementary Fig. 29 *Operando* XAS spectra of FeO_x/Ni-Ag during NO_3RR. (a) Ni *K*-edge XANES, (b) Ni *K*-edge EXAFS, (c) Ag *K*-edge XANES, and (d) Ag *K*-edge EXAFS spectra acquired under NO_3RR conditions.

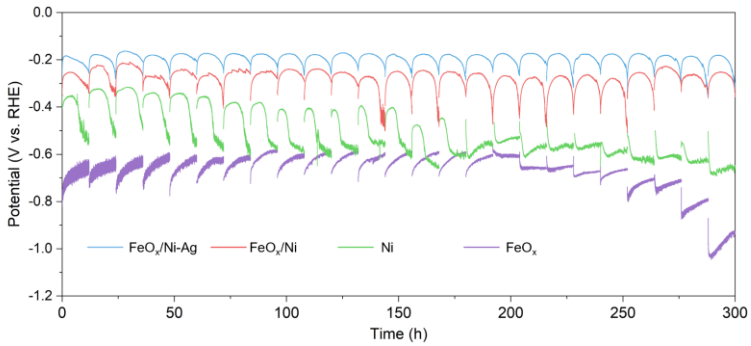

Supplementary Fig. 30 Potential-time profiles of the synthesized catalysts during continuous NO_3RR at 1 A cm^{-2} for 300 h.

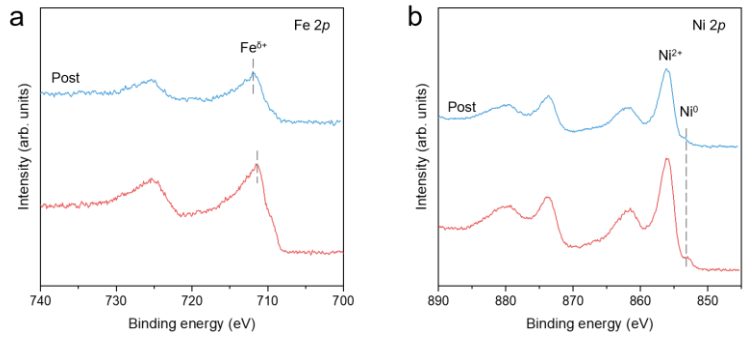

Supplementary Fig. 31 High-resolution XPS spectra before and after 300 h continuous NO_3RR at 1 A cm^{-2}: (a) Fe 2*p* spectra of FeO_x, and (b) Ni 2*p* spectra of Ni catalyst.

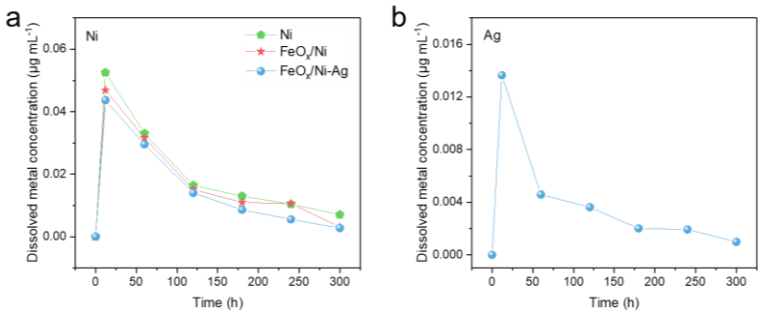

Supplementary Fig. 32 (a) Ni dissolution behavior of Ni catalyst, FeO_x/Ni and FeO_x/Ni-Ag, and (b) Ag dissolution behavior of FeO_x/Ni-Ag during continuous NO_3RR at 1 A cm^{-2}.

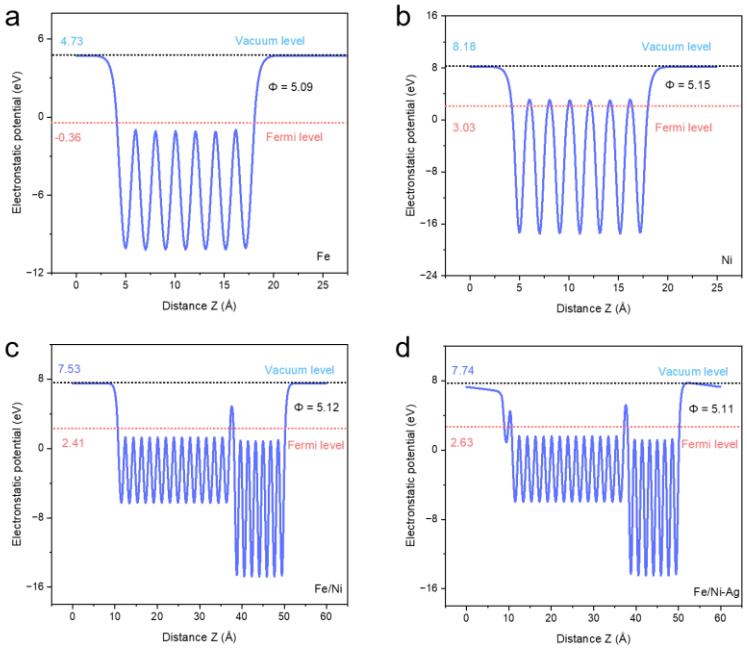

Supplementary Fig. 33 Work function calculations of (a) Fe, (b) Ni, (c)Fe/Ni, and Fe/Ni-Ag.

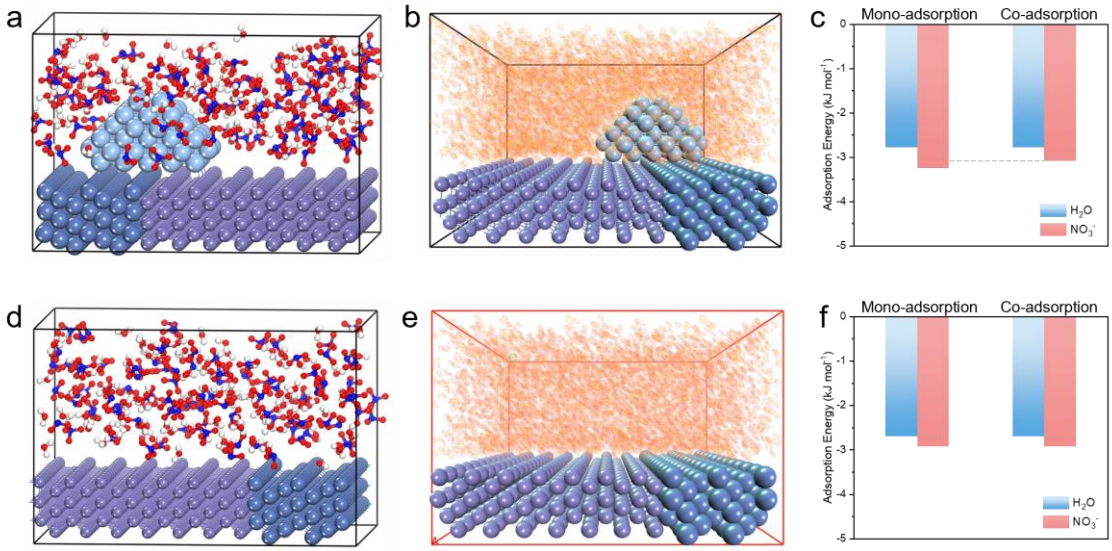

Supplementary Fig. 34 (a,b) Optimized adsorption configurations of H_2O and NO_3^- on Fe/Ni-Ag. (c) Comparison of adsorption energies of H_2O and NO_3^- on FeO_x/Ni-Ag under individual and co-adsorption configurations, calculated based on the models shown in (b). (d,e) Adsorption configurations of H_2O and NO_3^- on Fe/Ni. (f) Comparison of adsorption energies H_2O and NO_3^- on Fe/Ni under individual and co-adsorption configurations, calculated based on the models shown in (e).

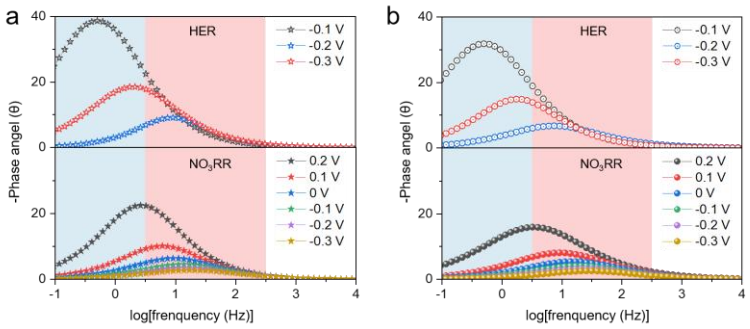

Supplementary Fig. 35 *In-situ* EIS Bode plots of (a) FeO_x/Ni and (b) FeO_x/Ni-Ag during HER and NO_3RR at different applied potentials.

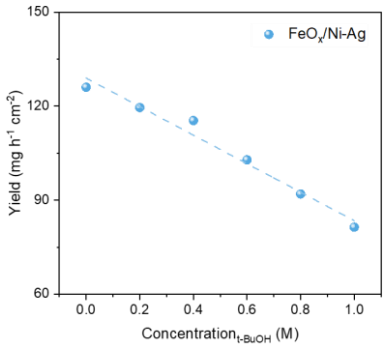

Supplementary Fig. 36 Effect of t-BuOH concentration on NH_3 production at -0.4 V (vs. RHE).

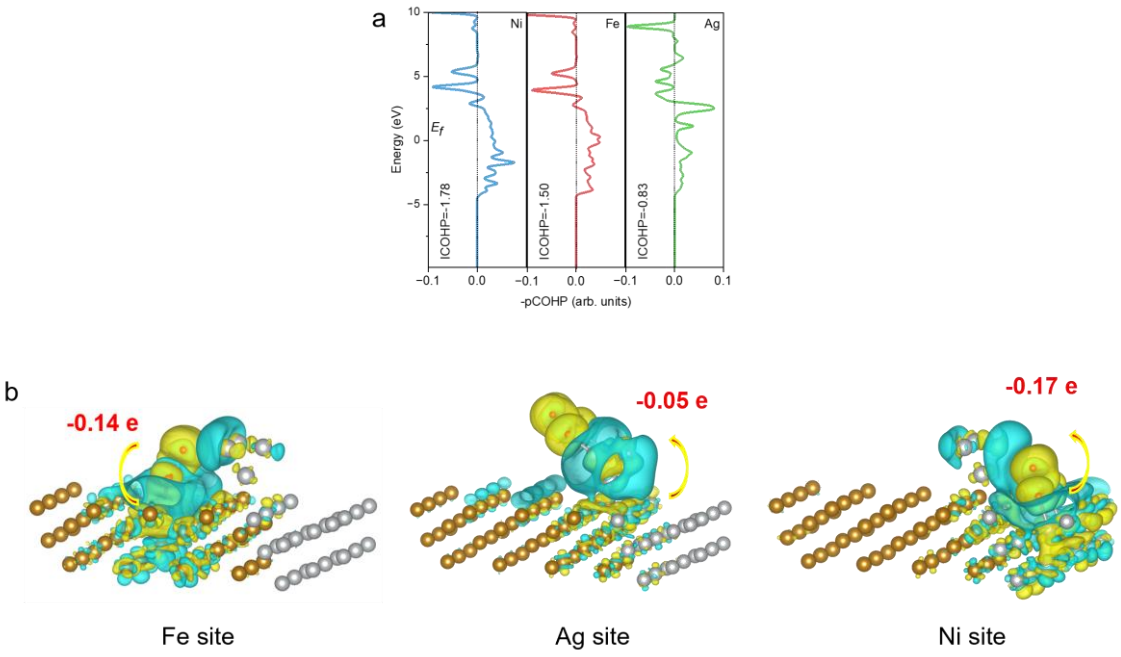

Supplementary Fig. 37 (a) pCOHP profiles showing NO_3^- adsorption on distinct interfacial sites of FeO_x/Ni-Ag. (b) Charge density difference of NO_3^- adsorption on different metal sites in FeO_x/Ni-Ag, where yellow and cyan denote electron accumulation and depletion.

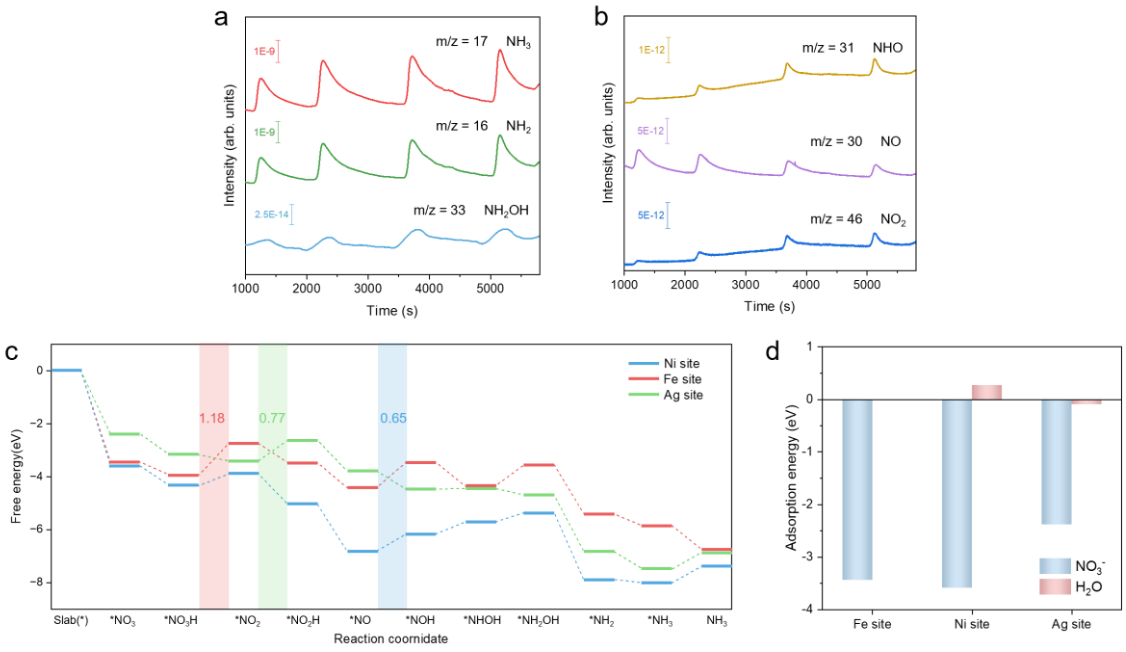

Supplementary Fig. 38 (a,b) Online DEMS spectra recorded for FeO_x/Ni-Ag during NO_3RR. (c) DFT calculated energy profiles for NO_3RR at different active sites of FeO_x/Ni-Ag. (d) Adsorption energies of NO_3^- and H_2O at different active sites of FeO_x/Ni-Ag.

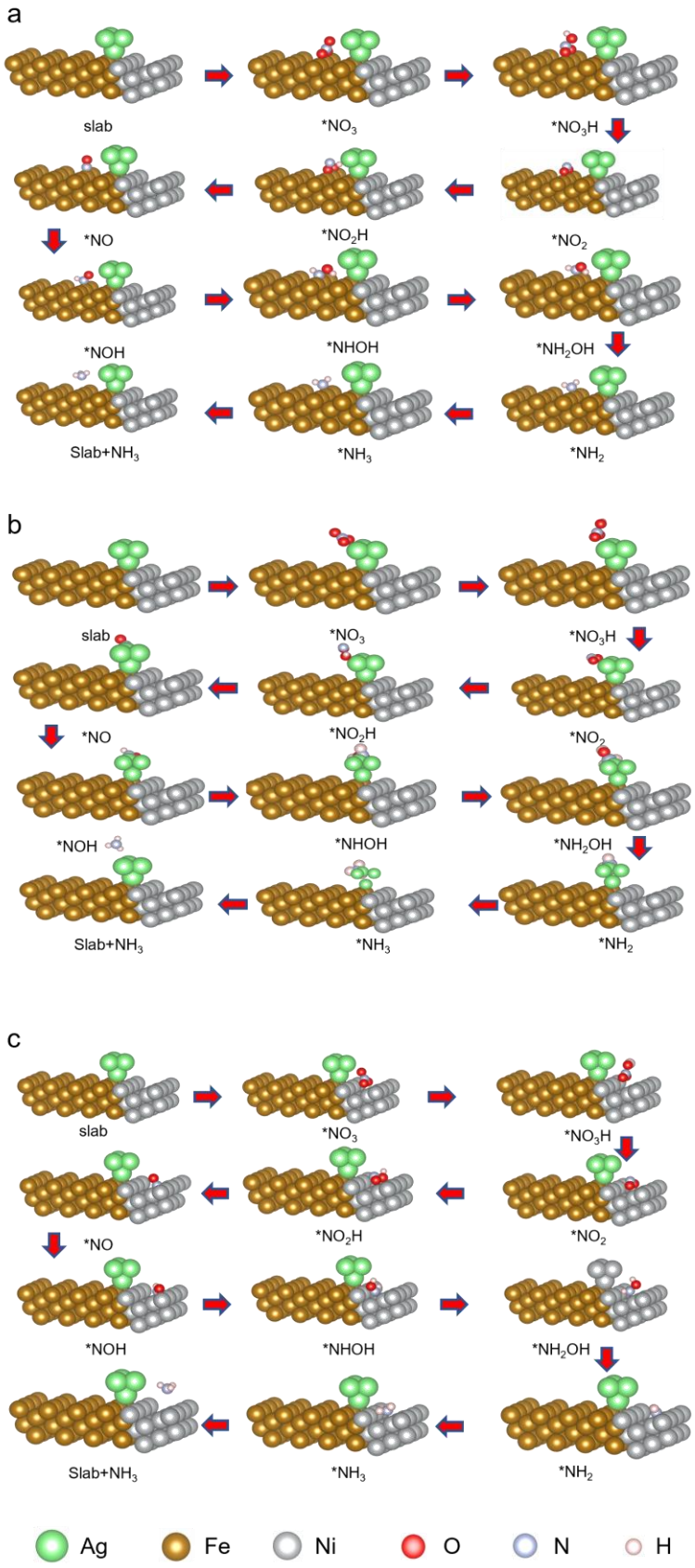

Supplementary Fig. 39 Adsorption configurations of NO_3RR intermediates on FeO_x/Ni-Ag at (a) Fe, (b) Ag, and (c) Ni sites.

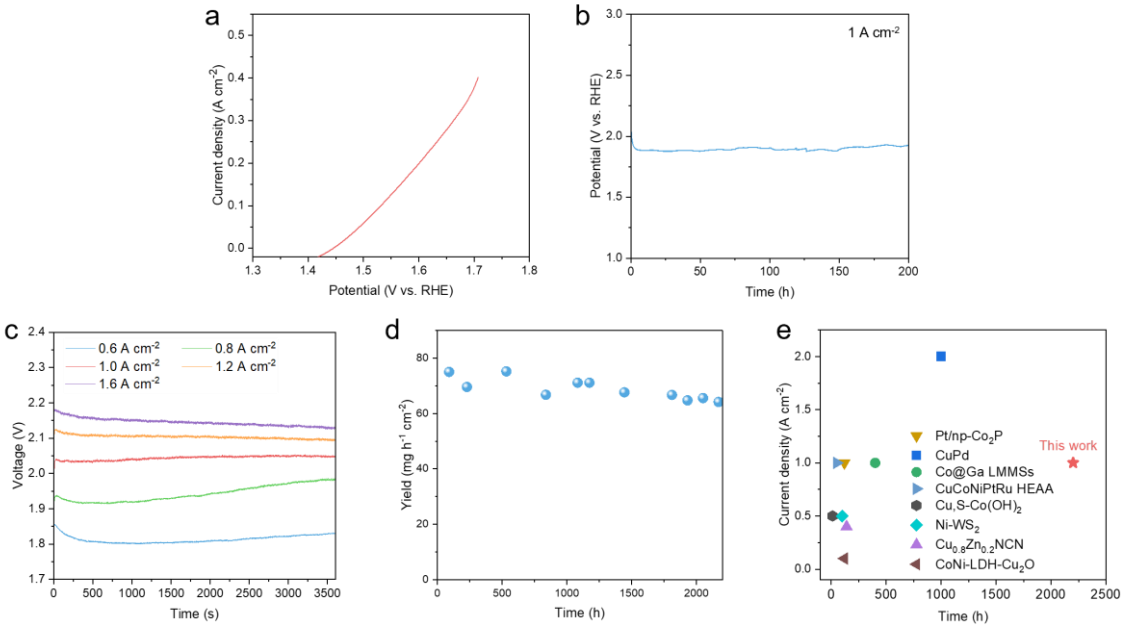

Supplementary Fig. 40 Electrochemical OER and MEA performance of FeO_x/Ni-Ag. a,b, OER measurements in a three-electrode configuration: (a) LSV curves and (b) potential-time response at 1 A cm^{-2}. c-e, MEA performance using FeO_x/Ni-Ag as both cathode and anode: (c) voltage-time curves at various current densities; and (d) NH_3 yield rate during long-term operation. (e) Comparison of MEA NO_3RR performance for reported catalysts.

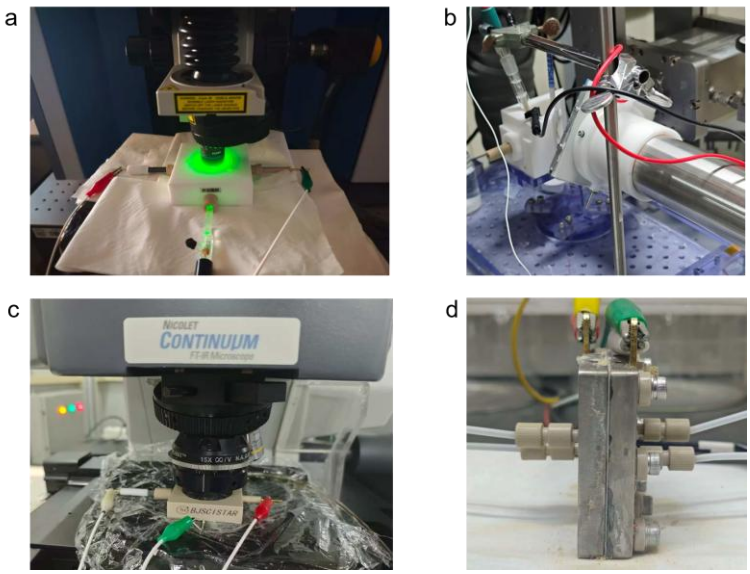

Supplementary Fig. 41 Photographs of experimental setups for (a) *In-situ* Raman, (b) *operando* XAS, (c) *In-situ* SR-FTIR measurements, and (d) MEA system.

Supplementary Table 1 Descriptors included in the Pearson correlation analysis.

Category	Property	Abbreviation
Periodic properties	Atomic radius	r
	Atomic number	N
	Atomic mass	m
	Period number	Np
	Electronegativity	χ
Crystallographic	Lattice constant	a
	Single atomic energy	E_{atom}
	Binding energy	$E_{binding}$
	Valence electron number	V_E
	Electron affinity	E_{aff}
Reactive properties	Bond length to H	R_{TM-H}
	Adsorption energy to H	G_{ads-H}
	Bond length to OH	R_{TM-OH}
	Adsorption energy to OH	G_{ads-OH}
	d-band center	ε_d
	COHP	ICOHP

Supplementary Table 2 Atomic ratios of different elements in FeO_x/Ni-Ag determined by ICP-OES.

Fe	Ni	Ag
8.41 at%	24.29 at%	0.20 at%

Supplementary Table 3 Performance comparison between FeO_x/Ni-Ag and recently reported advanced NO_3RR catalysts.

Catalyst	Electrolyte	FE_{max} (%)	$Yield_{max}$ (FE>90%) (mg h^{-1} cm^{-2})	Stability (h)	Refences
FeO_x/Ni-Ag	1 M KOH + 1 M KNO_3	97.43	149.24	1357	This work
Pd1/CuS	1 M KOH + 0.5 M KNO_3	~100	17.22	90	Ref. 27
La-CuOx	1 M KOH + 1 M KNO_3	99.74	140	10	Ref. 28
Co@Ga LMMSs	1 M NaOH + 1 M $NaNO_3$	99.59	12.17	400	Ref. 29
PCN-Cu-DAC	1 M KOH + 1 M KNO_3	97.5	25.80	360	Ref. 30
Ov-Co(OH)2/Cu	1 M KOH + 0.5 M KNO_3	97.	167.8	25	Ref. 31
p-CN-$Cu^{s}La^{n}$-*m*	1 M KOH + 0.5 M KNO_3	97.7	37.55	110	Ref. 32
NiMnCoAg-BHT	1 M KOH + 1 M KNO_3	98	36.23	10	Ref. 33

4H/fcc Au-Cu	1 M KOH + 1 M KNO_3	98.9	116.2	16	Ref. 34
Co3O4/Cu-N-C	1 M KOH + 1 M KNO_3	97.7	109.84	20	Ref. 35
SD-Fe1-Ti	1 M KOH + 1 M KNO_3	95.2	68.12	20	Ref. 36
NiCoP	1 M KOH + 1 M KNO_3	99.7	110.37	24	Ref. 37
Cu1Co1-HDS	1 M KOH + 0.5 M KNO_3	96.15	78.78	20	Ref. 38
Cu1Co5	1 M KOH + 1 M KNO_3	96.2	32.4	30	Ref. 39
CuPc MDE	1 M KOH + 1 M KNO_3	98.4	62.4	30	Ref. 40
CuNi NPs	1 M KOH + 0.71 M KNO_3	97.03	94.57	12	Ref. 41

Supplementary Table 4 MEA performance comparison between FeO_x/Ni-Ag and recently reported advanced NO_3RR catalysts.

Catalyst	Electrolyte	Voltage in 1 A cm^{-2} (V)	FE in 1 A cm^{-2} (%)	Current density for stability test (A cm^{-2})	Durability (h)	Refences
FeO_x/Ni-Ag	1 M KOH + 1 M KNO_3	2.04	90.5	1	2200	This work
Pt/np-Co_2P	1 M KOH + 1 M KNO_3	2.15	96.6	1	120	Ref. 42
CuPd	1 M KOH + 1 M KNO_3	2.21	80.4	2	1000	Ref. 43
Co@Ga LMMSs	1 M NaOH + 1 M $NaNO_3$	2.20	90.0	1	400	Ref. 29
CuCoNiPtRu HEAA	1 M KOH + 0.5 M KNO_3	2.20	93.8	1	50	Ref. 44
Cu,S-$Co(OH)_2$	1 M KOH + 0.1 M KNO_3	2.10	81.3	0.5	12	Ref. 45
Ni-WS_2	1 M KOH + 0.1 M KNO_3	/	/	0.5	100	Ref. 46
$Cu_{0.8}Zn_{0.2}NCN$	1 M KOH + 0.5 M KNO_2	2.30	67.71	0.4	140	Ref. 47
CoNi-LDH-Cu_2O	1 M KOH + 0.1 M KNO_3	/	/	0.1	120	Ref. 48

Reference

1. Kresse, G. & Hafner, J. Ab initio molecular dynamics for liquid metals. *Phys. Rev. B* **47**, 558-561 (1993).
2. Kresse, G. & Furthmüller, J. Efficiency of ab-initio total energy calculations for metals and semiconductors using a plane-wave basis set. *Comp. Mater. Sci.* **6**, 15-50 (1996).
3. Blöchl, P.E. Projector augmented-wave method. *Phys. Rev. B* **50**, 17953-17979 (1994).
4. Kresse, G. & Joubert, D. From ultrasoft pseudopotentials to the projector augmented-wave method. *Phys. Rev. B* **59**, 1758-1775 (1999).
5. Perdew, J.P., Burke, K. & Ernzerhof, M. Generalized Gradient Approximation Made Simple. *Phys. Rev. Lett.* **77**, 3865-3868 (1996).
6. Kresse, G. & Furthmüller, J. Efficient iterative schemes for ab initio total-energy calculations using a plane-wave basis set. *Phys. Rev. B* **54**, 11169-11186 (1996).
7. Monkhorst, H.J. & Pack, J.D. Special points for Brillouin-zone integrations. *Phys. Rev. B* **13**, 5188-5192 (1976).
8. Grimme, S. Semiempirical GGA-type density functional constructed with a long-range dispersion correction. *J. Comput. Chem.* **27**, 1787-1799 (2006).
9. Mathew, K., Sundararaman, R., Letchworth-Weaver, K., Arias, T.A. & Hennig, R.G. Implicit solvation model for density-functional study of nanocrystal surfaces and reaction pathways. *J. Chem. Phys.* **140**, 084106 (2014).
10. Henkelman, G., Arnaldsson, A. & Jónsson, H. A fast and robust algorithm for Bader decomposition of charge density. *Comp. Mater. Sci.* **36**, 354-360 (2006).
11. Bader, R.F.W. A quantum theory of molecular structure and its applications. *Chem. Rev.* **91**, 893-928 (1991).
12. Dronskowski, R. & Bloechl, P.E. Crystal orbital Hamilton populations (COHP): energy-resolved visualization of chemical bonding in solids based on density-functional calculations. *J. Phys. Chem.* **97**, 8617-8624 (1993).
13. Maintz, S., Deringer, V.L., Tchougréeff, A.L. & Dronskowski, R. LOBSTER: A tool to extract chemical bonding from plane-wave based DFT. *J. Comput. Chem.* **37**, 1030-1035 (2016).
14. Nosé, S. A unified formulation of the constant temperature molecular dynamics methods. *J. Chem. Phys.* **81**, 511-519 (1984).
15. Zhao, X. & Liu, Y. Origin of Selective Production of Hydrogen Peroxide by Electrochemical Oxygen Reduction. *J. Am. Chem. Soc.* **143**, 9423-9428 (2021).
16. Nørskov, J.K. et al. Trends in the Exchange Current for Hydrogen Evolution. *J. Electrochem. Soc.* **152**, J23 (2005).
17. Shi, X. et al. Revealing and modulating catalyst reconstruction for highly efficient electrosynthesis of ammonia. *Nat. Commun.* **16**, 6161 (2025).
18. Ly, A., Marsman, M. & Wagenmakers, E.-J. Analytic posteriors for Pearson's correlation coefficient. *Stat. Neerl.* **72**, 4-13 (2018).
19. Hao, J. & Ho, T.K. Machine Learning Made Easy: A Review of Scikit-learn Package in Python Programming Language. *J. Edu. Behav. Stat.* **44**, 348-361 (2019).
20. Jerome, H.F. Greedy function approximation: A gradient boosting machine. *Ann. Stat.* **29**, 1189-1232 (2001).
21. Belgiu, M. & Drăguţ, L. Random forest in remote sensing: A review of applications and future directions. *ISPRS J. Photogram. Remote Sens.* **114**, 24-31 (2016).
22. Peterson, L.E. K-nearest neighbor. *Scholarpedia* **4**, 1883 (2009).

23. Dey, P., Nag, K., Pal, T. & Pal, N.R. Regularizing Multilayer Perceptron for Robustness. *IEEE Trans. Sys. Man Cybern. Syst.* **48**, 1255-1266 (2018).
24. Ding, Y., Tong, L., Liu, X., Liu, Y. & Zhao, Y. Artificial Intelligence-Driven Innovations in Hydrogen Storage Technology. *Energy Environ. Mater.* **8** (2025).
25. Ouyang, R., Curtarolo, S., Ahmetcik, E., Scheffler, M. & Ghiringhelli, L.M. SISSO: A compressed-sensing method for identifying the best low-dimensional descriptor in an immensity of offered candidates. *Phys. Rev. Mater.* **2**, 083802 (2018).
26. Purcell, T.A.R., Scheffler, M. & Ghiringhelli, L.M. Recent advances in the SISSO method and their implementation in the SISSO++ code. *J. Chem. Phys.* **159**, 114110 (2023).
27. He, Q. et al. Dynamic Reconstruction and Microenvironment Modulation of a Pd-Doped CuS Electrocatalyst for Nearly Unity-Efficiency Ammonia Electrosynthesis from Nitrate. *J. Am. Chem. Soc.* **147**, 43067-43076 (2025).
28. Zhang, S. et al. Artificial Frustrated Lewis Pairs for Ampere-Level Ammonia Synthesis and High-Power-Density Zinc-Nitrate Battery. *J. Am. Chem. Soc.* **147**, 41433-41442 (2025).
29. Chen, W. et al. Liquid Metal Dynamic Interface Enabled Reverse Hydrogen Spillover Boosting Electrocatalytic Nitrate Reduction. *Angew. Chem. Int. Ed.* **65**, e202516997 (2026).
30. Li, Q., Li, Y., Xu, B., Yang, J. & Wang, Y. Gram-Scale Ammonia Synthesis via Electrochemical Nitrate Reduction Using Enzyme-Inspired Dual-Atomic Cu Catalyst. *Angew. Chem. Int. Ed.* **64**, e202510139 (2025).
31. Mei, W. et al. Robust Oxygen-Vacancy-Engineered $Co(OH)_2$/Cu Heterostructures Boost Nitrate Electroreduction to Ammonia beyond 2 A cm^{-2}. *Adv. Mater.* **37**, 2507363 (2025).
32. Zuo, Y. et al. Capturing Copper Single Atom in Proton Donor Stimulated O-End Nitrate Reduction. *Adv. Mater.* **37**, 2415632 (2025).
33. Namvar, S. et al. 2D Multivariate-Metal-Organic Frameworks (2D-M^2OF) for High Yield Ammonia Synthesis from Nitrate. *Adv. Energy Mater.* **15**, 2405031 (2025).
34. Ma, Y. et al. Unconventional phase metal heteronanostructures with tunable exposed interface for efficient tandem nitrate electroreduction to ammonia. *Nat. Commun.* **16**, 7632 (2025).
35. Liu, Y. et al. Efficient tandem electroreduction of nitrate into ammonia through coupling Cu single atoms with adjacent Co_3O_4. *Nat. Commun.* **15**, 3619 (2024).
36. Dai, J. et al. Spin polarized Fe_1-Ti pairs for highly efficient electroreduction nitrate to ammonia. *Nat. Commun.* **15**, 88 (2024).
37. Li, Y. et al. Improved Nitrate-to-Ammonia Electrocatalysis through Hydrogen Poisoning Effects. *Angew. Chem. Int. Ed.* **63**, e202411068 (2024).
38. Jang, W. et al. Homogeneously Mixed Cu-Co Bimetallic Catalyst Derived from Hydroxy Double Salt for Industrial-Level High-Rate Nitrate-to-Ammonia Electrosynthesis. *J. Am. Chem. Soc.* **146**, 27417-27428 (2024).
39. Zhou, Y. et al. Boosting Electrocatalytic Nitrate Reduction to Ammonia via Promoting Water Dissociation. *ACS Catal.* **13**, 10846-10854 (2023).
40. Jiang, Z. et al. Molecular electrocatalysts for rapid and selective reduction of nitrogenous waste to ammonia. *Energy Environ. Sci.* **16**, 2239-2246 (2023).
41. Yu, W. et al. Laser-controlled tandem catalytic sites of CuNi alloys with ampere-level electrocatalytic nitrate-to-ammonia reduction activities for Zn-nitrate batteries. *Energy Environ. Sci.* **16**, 2991-3001 (2023).
42. Zhou, X. et al. Tuning Active Hydrogen via Spillover Enables the Wide-Potential Electrochemical

Reduction of Nitrate to Ammonia. *Adv. Mater.* e18272 (2025). https://doi.org/10.1002/adma.202518272
43. Fu, Y. et al. Copper-palladium hydride interfaces promote electrochemical ammonia synthesis. *Nat. Synth.* (2025). https://doi.org/10.1038/s44160-025-00941-1
44. Li, S. et al. A Reaction-Diffusion-Coupled Strategy for Ampere-Level Electrocatalytic Nitrate Reduction to Ammonia. *Nano Lett.* **25**, 14185-14194 (2025).
45. Yu, F. et al. Dual Ion Leaching-Induced Reconstruction of $CuCo_2S_4$ Boosts Electrocatalytic Nitrate Reduction to Ammonia with Favorable Active Hydrogen Coverage. *Adv. Energy Mater.* **15**, e03613 (2025).
46. Lv, J. et al. Accelerating Nitrate Electroreduction to Ammonia via Metal-Support Interactions in Ni-WS_2 Catalysts. *J. Am. Chem. Soc.* **147**, 27708-27719 (2025).
47. Wang, J.J. et al. A Copper-Zinc Cyanamide Solid-Solution Catalyst with Tailored Surface Electrostatic Potentials Promotes Asymmetric N-Intermediate Adsorption in Nitrite Electroreduction. *J. Am. Chem. Soc.* **147**, 8012-8023 (2025).
48. Zheng, M., Wan, Y., Huang, Z.-H., Kang, F. & Lv, R. Interfacial Synergistic Hydrogen Spillover and Electron Transfer for Boosting Electrocatalytic Nitrate Reduction to Ammonia. *Adv. Mater.* **38**, e14834 (2026).